

3. Results of Flight Scientific Programmes, Research and Observation Realized (Implemented) in 2013-2015

1.1.1 Creation of new instruments and continuation of sets of observations

The Radio Astrophysical Observatory (RAO) of the ISTP SB RAS has already mounted a multi-wave radioheliograph at 4–8 GHz (Fig. 1). We got the first radio images of the Sun at three wavelengths simultaneously (Fig. 2).



Fig. 1. The RAO main view. Cross-shaped central part of the array is the multi-wave radioheliograph at 4–8 GHz.

The observatory also has auxiliary instruments:

- a) spectropolarimeter at 4–8 GHz with time resolution of up to 10 m/s, 26 frequency channels, and frequency band of channels of 50 MHz.

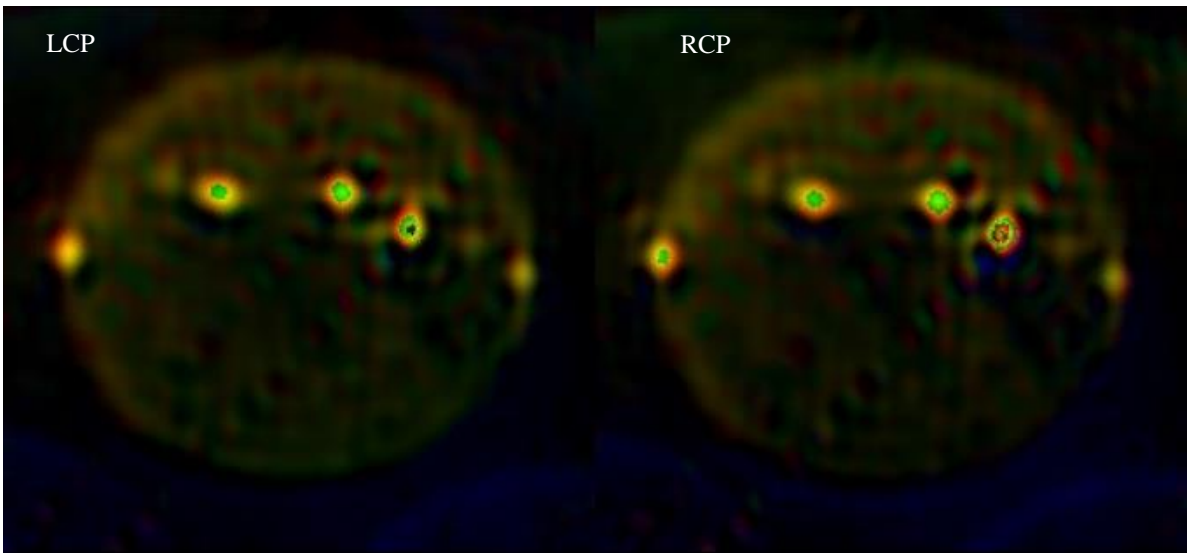


Fig. 2. Compound images of the Sun at 5, 6 and 7 GHz from the multi-wave radioheliograph on May 2, 2016 in the left (LCP) and right (RCP) circular polarization. Green color corresponds to 5 GHz; red one, to 6 GHz; blue one, to 7 GHz.

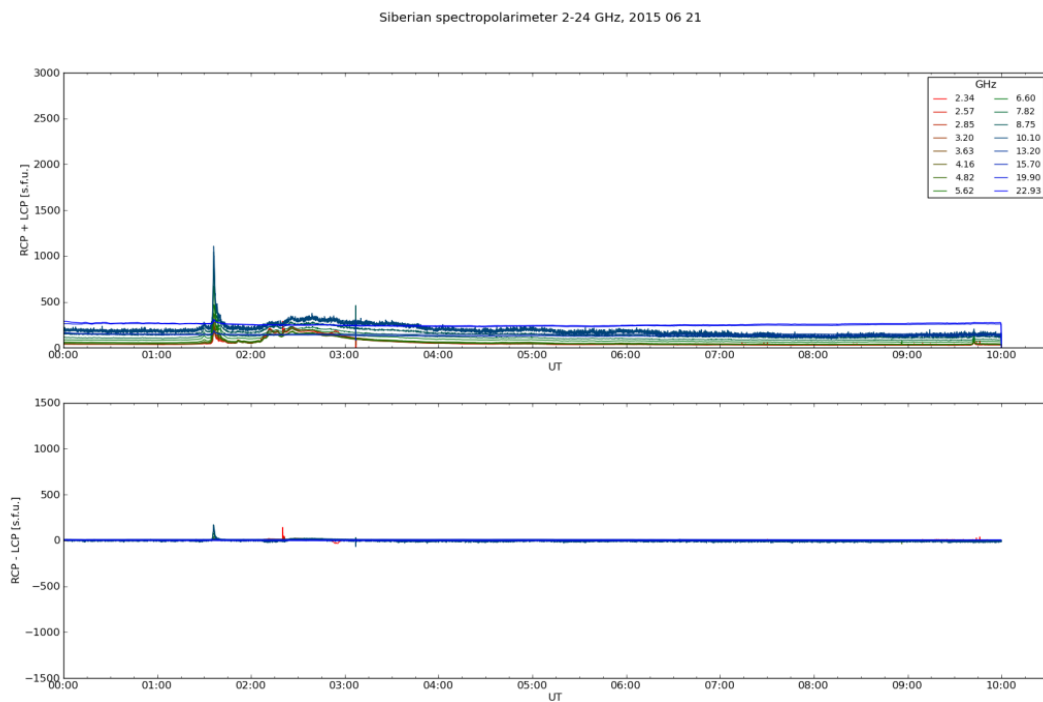


Fig. 3. June 21, 2015 solar flare recorded by spectropolarimeter in intensity (I, top) and circular polarization (bottom) at 2–24 GHz.

b) spectropolarimeter at 2–24 GHz, with signal integration time in one frequency channel of up to 0.1 seconds, frequency resolution of 50 MHz. The number of channels depends on the objective. A normal operation mode uses 16

channels. We can obtain dynamic spectra of broadband bursts of solar microwave radiation at 2–24 GHz. Regular daytime observations are carried out; their results are processed and stored in processed form, as well as in their original form. Fig. 3 illustrates June 21, 2015 solar flare in intensity at different frequencies of 2–24 GHz and circular polarization.

The multi-wave radioheliograph is calibrated against geostationary satellites, the Moon. We are developing methods for reconstruction of the images obtained at the multi-wave radioheliograph.

We continue a multi-year set of observations with the SSRT and spectropolarimeters at 2–24, 4–8 GHz, providing an open access to data published on the observatory site (<http://badary.iszf.irk.ru>).

Publications:

Lesovoi S.V., Altyntsev A.T., Ivanov E.F., Gubin A.V. A 96-antenna radioheliograph // *Research in Astronomy and Astrophysics*, 2014. V. 14, Issue 7, Pp. 864-868.

Zhdanov D.A., Zandanov V.G. Observations of microwave fine structures by the Badary Broadband Microwave Spectropolarimeter and the Siberian Solar Radio Telescope // *Solar Phys.* 2015. V. 290. Pp. 287–294.

1.1.2 Synthesis of synoptic maps

For the first time, we synthesized synoptic maps of solar radio emission at 5.7 GHz in intensity and circular polarization. The maps are created on the basis of long-term solar observations made with the Siberian Solar Radio Telescope from 1998 to 2013. These maps are longitude-latitudinal distributions (Fig. 4) of solar microwave radiation in the 23rd and 24th solar cycles and contain new information about features of active region emission, large-scale thermal radio

radiation sources, prominences in the solar corona. In general, microwave radiation distribution in the solar cycles corresponds to long-term magnetographic and optical observations. The developed methods will be used in synoptic monitoring on new multi-wave SSRT radioheliograph.

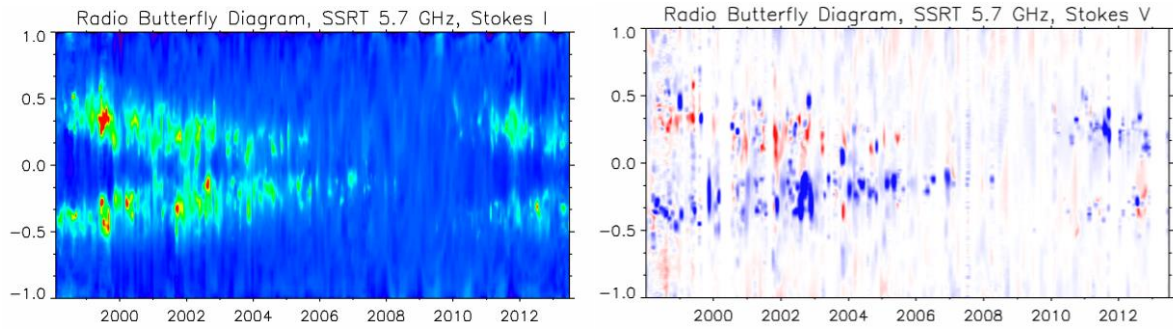


Fig. 4. Microwave (5.7 GHz) synoptic map for solar cycles 23, 24: the left panel shows Stokes parameter I; the right panel, Stokes parameter V.

1.1.3. Interpretation of anomalous polarization of AR radio emission

We interpreted anomalous polarization of radio emission according to the SSRT and reconstructed coronal magnetic field data. Supposing that radio emission passing through this region changes the polarization signal, we simulated radio emission, using information about the reconstructed field as one of the input parameters.

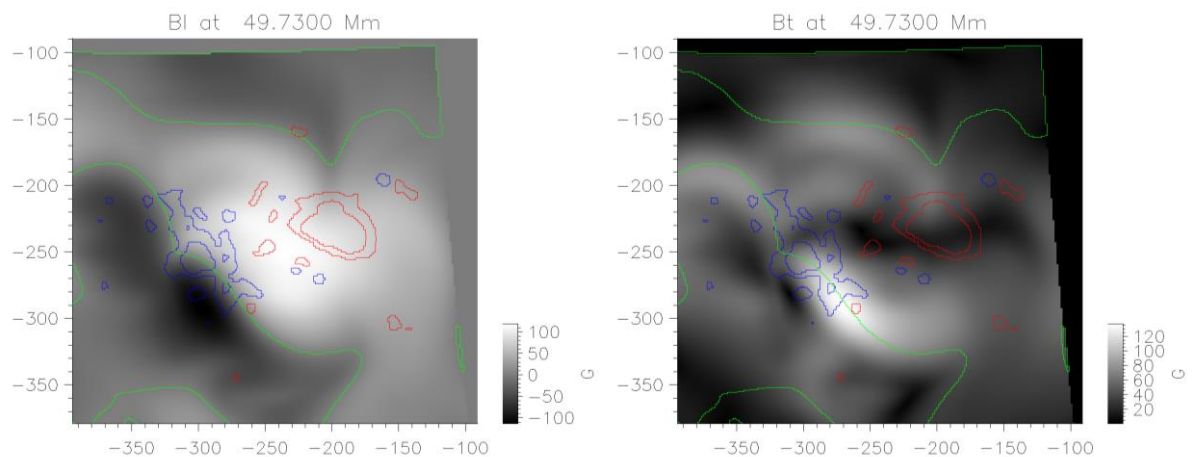


Fig. 5. The perpendicular of the line-of-sight projection of the reconstructed magnetic field at the height about 50 Mm, May 4 2013, 05:00 UT. The left panel depicts the component of the magnetic field along the line-of-sight (longitudinal); the right panel, the absolute value of the transverse component of the magnetic field. The blue and red contours mark negative and

positive polarity at the level of the photosphere, respectively. The neutral line at the specified height is shown by green color.

The simulated radio emission maps repeat the registered spatial polarization structure. The potential field did not allow us to match observations with simulations (Fig. 5).

Publications:

Kalman T.I., Kochanov A.A., Myshyakov I.I., Maksimov V.P., Prosovetsky D.V., Tokhchukova S.Kh. Observations and simulations of spatial distribution and the spectrum of microwave radiation of active region NOAA 11734 (in Russian) // *Geomagnetism and Aeronomy*. 2015. V. 55, N. 8. Pp. 1–7.

1.1.4. Relations between microwave bursts and near-Earth proton increases

We found relations between microwave bursts and near-Earth proton increases of high energies and their origin. We continued study of relationships between parameters of bursts at 35 GHz recorded by Nobeyama Radio Heliograph within 25 years and solar proton events. We studied relations between microwave fluences at 35 GHz and fluences of near-Earth proton increases with energies higher than 100 MeV for revelation of information about their sources and evaluation of diagnostic potential of radio bursts.

The correlation between microwave and proton fluences is significantly higher than between peak values (Fig. 6). This could reflect a dependence of the total proton number on the duration of their acceleration. In the events with energetic flares, the correlation coefficients of high-energy proton fluences and fluences of microwave and soft X-ray radiation are higher than that with CME velocities (fig. 7).

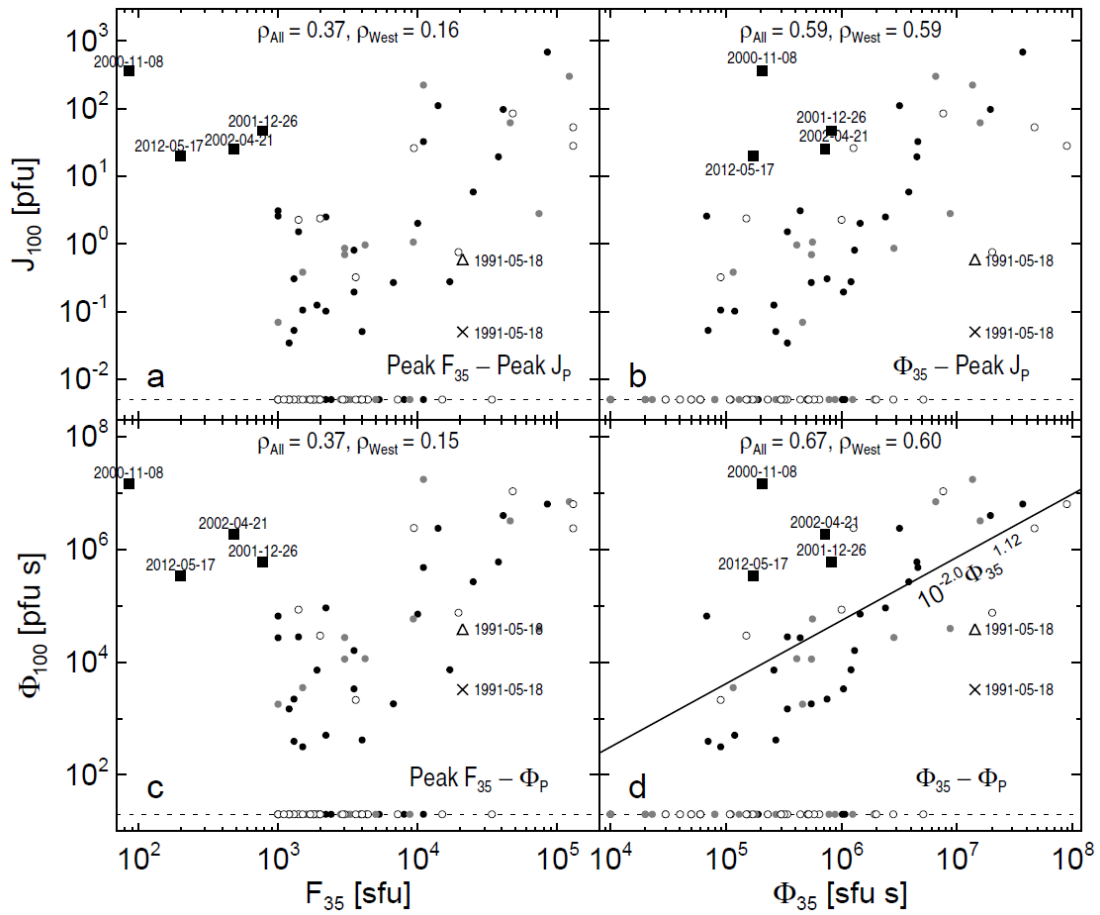


Fig.6. The statistical relations between different combinations of the peak fluxes and fluences of microwave bursts at 35 GHz and proton increases > 100 MeV. The energetic protonic events after moderate microwave bursts are marked with the filled black squares. The longitude of the solar source is coded by the color: open is for $l < E30$; gray, $E30 < l < W20$; black, $l > W20$. The Pearson correlation coefficients specified in each panel were calculated separately for all events presented (ρ_{All}) and for the western events only (ρ_{West}). The latter events are lower, because all of the atypical events were caused by western sources.

These results indicate statistically greater contribution of flare processes to protons fluxes of high energies.

Acceleration with shock waves could be less significant for high energies in the events related to energetic flares, although their contribution is likely and might prevail in less pronounced events. We found that probability of an observed proton increase directly depended on a maximum flux, duration, and fluence of a burst at 35 GHz. The role of "the large flare syndrome" was earlier strongly exaggerated. We suggested empirical relationships for microwave diagnostics of protons increases.

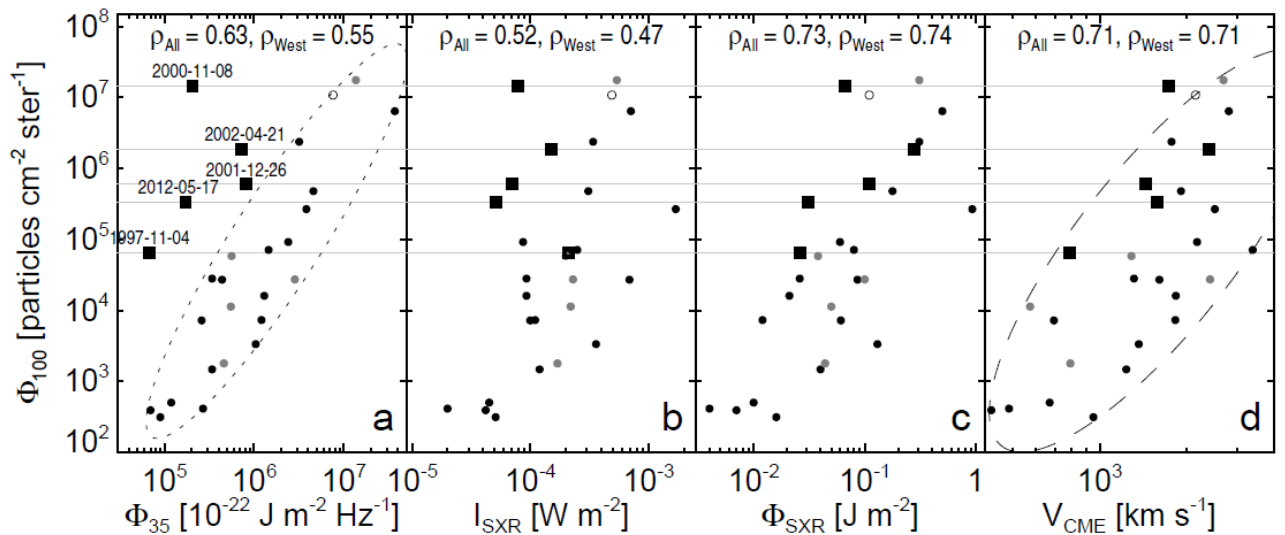


Fig. 7. The scatter (log–log) plots of longitude-corrected proton fluence versus microwave fluence (a), peak soft X-ray flux (b) and fluence (c), and CME speed (d). The symbols are the same as in Fig. 6.

Publications:

Grechnev V.V., Kiselev V.I.; Meshalkina N.S., Chertok I.M. Relations between microwave bursts and near-Earth high-energy proton enhancements and their origin // *Solar Physics*. 2015. V. 290. Pp. 2827–2855.

1.1.5. Analysis of flare observation data

Analysis of a series of flare observations whose continual emission had polarization inverse at 17–34 GHz showed that circulation was associated with pitch-angle anisotropy of emitting electrons.

Publications:

Altyntsev A.T., Fleishman G.D., Kashapova L.K., Meshalkina N.S., Myshyakov I.I. Palshin V.D. Two-loop flare SOL2012-07-06: relationship between heating, acceleration and circular polarization sign inversion in microwaves // *RadioSun-4 Workshop*, 8–12 June 2015, ISTP, Irkutsk, Russia).

1.1.6. A software package for microwave and x-radiation simulation

We developed software packages allowing us to simulate microwave and x-radiation. The software architecture developed on the basis of IDL enables the user to: 1) import photospheric magnetic fields and extrapolate them into the solar corona; 2) study magnetic topology of interactive magnetic field lines and magnetic loops associated with them; 3) fill loops with heterogeneous plasma and accelerated electrons with given parameters; 4) study spatial and spectral characteristics of radio emission and x-radiation; 5) compare simulated and observed images. The software integrates gyrosynchrotron and deceleration microwave radiation calculation, soft and hard X-ray radiation calculation, extrapolation program codes into the coronal magnetic field in a linear and nonlinear force-free approximation. The software was tested by relatively simple one-loop configurations.

Publications:

Kuznetsov A.A., Van Doorselaere T., Reznikova V.E. Simulations of gyrosynchrotron microwave emission from an oscillating 3d magnetic loop // *Solar Physics*. 2015. V. 290, iss. 4. Pp. 1173–1194.

Nita G.M., Fleishman G.D., Kuznetsov A.A., Kontar E.P., Gary D.E. Three-dimensional radio and X-ray modeling and data analysis software: revealing flare complexity // *Astrophys. J.* 2015. V. 799. Id. 236. P. 15.

Reznikova V.E., Van Doorselaere T., Kuznetsov A.A. Perturbations of gyrosynchrotron emission polarization from solar flares by sausage modes: forward modeling // *Astronomy & Astrophysics*. 2015. V. 575. Id. A47, P. 9.

1.1.7. On injection and effects of motion of non-thermal electrons

We obtained results on injection and effects of proliferation of non-thermal electrons. After analyzing a one-loop flare on May 21, 2004, we compared microwave observations with the simulated data calculated, using GX Simulator based on an IDL technique. Comparative analysis allowed us to define spatial and spectral properties of a distribution of non-thermal electrons. We found that emission was generated by high-energy electrons with a relatively hard spectrum concentrated close to the top of the loop. At the same time, the flux of electrons with the energy more than 100 keV close to the foot was too small to be recorded in an integral flux and RHESSI images. The SOHO images at vacuum UV wavelength and features of a low frequency part of microwave spectra suggest that the flare loop is submerged into a medium with smaller magnetic field. Most likely, the distribution of energetic electrons in the considered flare results from localized acceleration/injection of electrons at the top of the loop with the subsequent capture and scatter.

Publications:

Kurt V.G., Yushkov B.Yu., Kudela K., Galkin V.I., Kashapova L.K. CORONAS-F observation of HXR and gamma-ray emissions from the solar flare X10 on 29 October 2003 as a probe of accelerated proton spectrum // Contributions of the Astronomical Observatory SkalnatéPleso. 2015. V. 45. Pp. 42–59.

1.1.8. Simulation of microwave radiation of a solar active region

We carried out microwave observations of the solar active region NOAA 11734 from April 28 to May 8, 2013 from the SSRT and RATAN-600 (Fig. 8) radio telescopes.

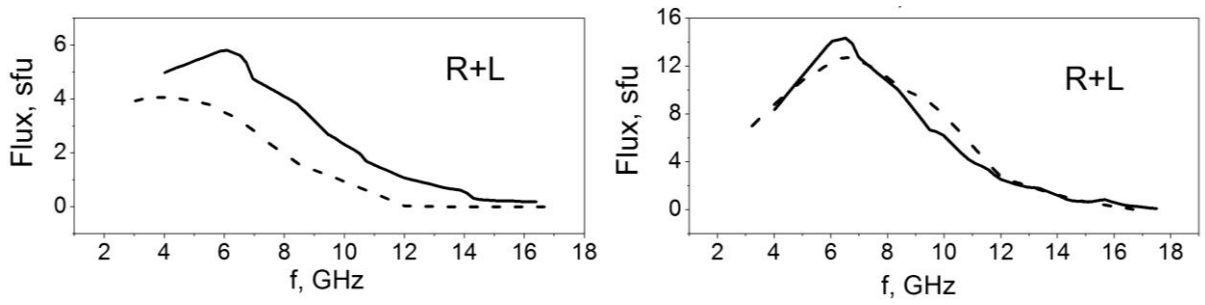


Fig. 8. The spectra of AO 11734 radio emission for preceding (left panels) and leading (right panels) sunspots: the solid curve shows the spectrum as inferred from RATAN-600; the dashed curve, a simulated result.

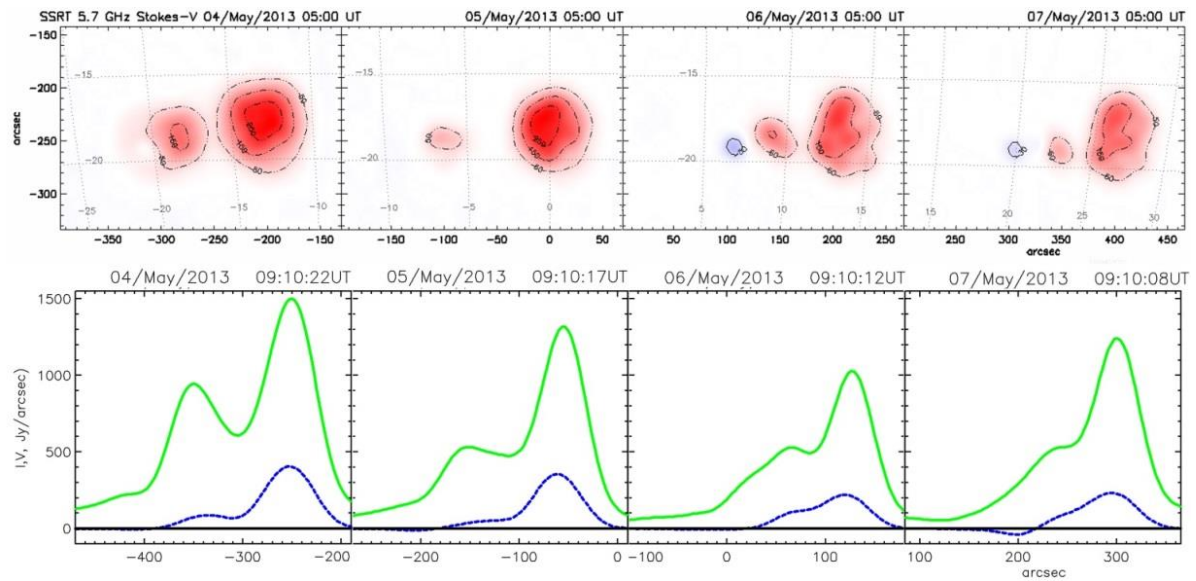


Fig. 9. The two-dimensional brightness temperature map (Stokes V) obtained from the SSRT (5.7 GHz) for positive (red) and for negative (green) values. The bottom panel shows one-dimensional response from the RATAN-600 at 5.7 GHz for the Stokes I (green line) and for the Stokes V (blue line) on May 4, 5, 6, 7 2013.

We got two-dimensional distributions of Stokes I and V parameters (Fig. 9) based on the data from the SSRT at 5.7 GHz and spectra of microwave radiation at 3–18 GHz from RATAN-600. We reconstructed the magnetic field in nonlinear force-free approximation, simulated free-free and gyroresonance radio emission.

We designed maps of simulation distribution of brightness temperatures for both circular polarizations of radio emission which repeated the registered spatial polarization structure on all the observation days. Analysis of observations and simulations of radio emission allow us to explain features of the distribution of

polarized radiation in the framework of the mechanism of weak interaction of modes of radio emission in the quasi-transverse magnetic field above sunspots.

Publications:

Kalman T.I., Kochanov A.A., Myshyakov I.I., Maksimov V.P., Prosovetsky D.V., Tokhchukova S.Kh. Observations and simulations of spatial distribution and the spectrum of microwave radiation of active region NOAA 11734 (in Russian) // *Geomagnetism and Aeronomy*. 2015. V. 55, N. 8. Pp. 1124–1130.

1.1.9. Simulation of quiet solar radio emission

Using a realistic Bifrost MHD model of the solar atmosphere, we calculated polarized radio radiation of a region of the quiet Sun for 1.7–30 cm wavelength. Study of generation of radio emission of this region allowed us to estimate relative contribution of a thermal deceleration and cyclotron emission mechanisms and to reveal some peculiarities in a pattern of a distribution of brightness temperatures in a spatial scale of ~ 48 km. It turned out that the characteristics of calculated emission matched with the observations by the RATAN-600 and SSRT for the regions of the quiet Sun.

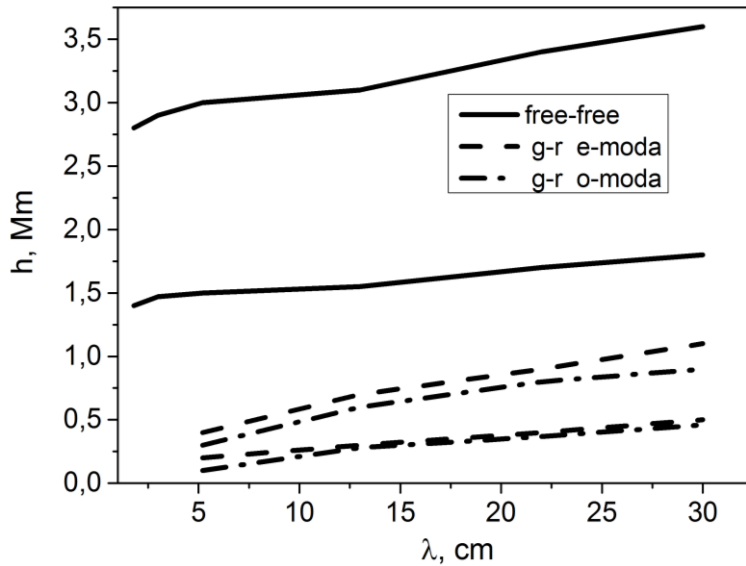


Fig. 10. The typical heights of generation of microwave radiation h (megameters, vertical axis) depending on wavelength λ (cm, horizontal axis).

As simulation showed, for this model, gyroresonance emission generated on the boundaries of granules up to 1 Mm was absorbed in overlying layers and is not accessible for observation.

Deceleration or free-free thermal radiation is optically-dense above all the calculated region with a large scatter of the typical heights where optical density is equal to unity (Fig. 10). Fine structure of deceleration emission depends on non-isotropic conditions in a three-dimensional region (Fig. 11). Contribution of this type of emission was $\sim 100\%$ for Bifrost model under consideration.

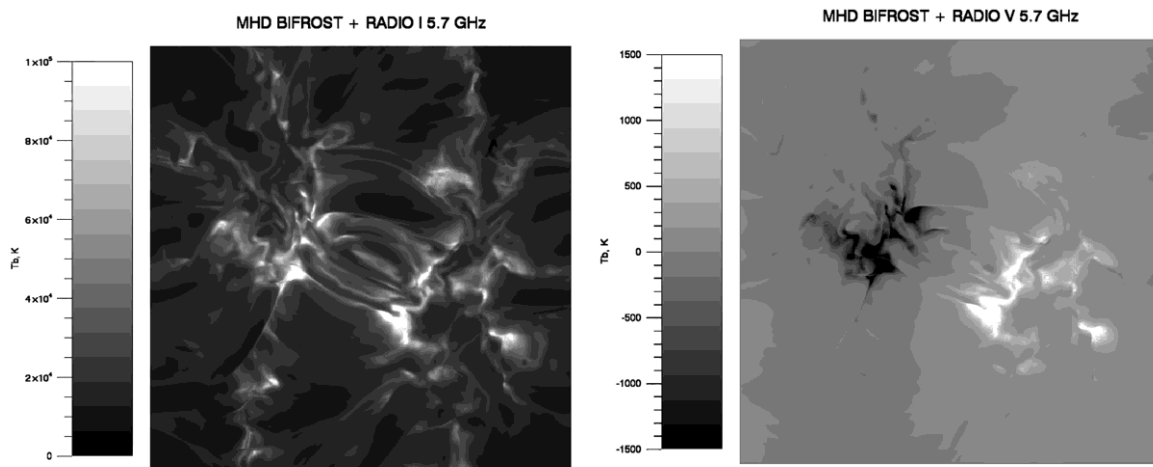


Fig. 11. The two-dimensional brightness temperature map (Stokes I, V) at 5.7 GHz for the Bifrost MHD simulation.

Publications:

Kalman T.I., Kochanov A.A. Study of characteristics and features of radio emission of an intensified chromospheric network using a realistic MHD model (in Russian) // The collection of scientific papers of the XIX Annual All-Russian Scientific Conference on Solar Physics "Solar Physics 2015", Pp. 189–192, ISBN 978-5-9651-0935-7.

1.1.10. Model of the quiescent corona emission in the range of 1–100 cm

We developed a model of the quiescent corona satisfying observations of radio wave emission in the range of 1–100 cm and intensity of coronal emission lines of the UV range. Yet we found a new solution of an equation of level population with stabilizing coefficients of a probabilistic character. Comparison of calculations and observations for a great number of emission lines showed their good match and allowed us to reveal a number of lines with inaccurate atom data, as well as demonstrated the need for correction of calculations of fractional ionization for one ion. The solution for a calculation of level population enables us to increase accuracy of plasma density diagnostics, determination of emission measure and temperatures of isothermal plasma. During calculations of intensity of coronal lines on the solar disk and over the limb, we used a dependence of redundancy of elements according to temperature and pressure in model coronal loops, which allowed us to determine average redundancy according to a line-of-sight in the near corona. This can be used for improvement of diagnostic procedures.

Publications:

Krissinel B. B. Simulation of the structure of quiet regions of the solar atmosphere corresponding to emission in 1–100 cm (in Russian) // An Astronomical Journal. 2015. V. 92, N. 1. Pp. 1–14.

1.1.11. Differences in the regimes of solar activity during global minima and beyond them

We suggested an explanation of a difference in the regimes of solar activity during global minima and beyond them. Two regimes of activity can be explained by hysteresis, presence of two solutions of dynamo equations with essentially different amplitudes of magnetic cycles implemented depending on initial conditions. The fluctuations of dynamo parameters lead to irregular transitions between different solutions. During the current year, hysteresis in dynamos has been confirmed by the three-dimensional numerical experiments which, however, were associated with high costs of machine time and did not allow us to calculate a sufficient number of magnetic cycles for determination of their statistical properties. A simple approximation of dynamo waves where we calculated about one million magnetic cycles whose amplitude-distribution function confirmed the existence of two modes for solar activity represents such a possibility.

Publications:

Karak B.B., Kitchatinov L.L., Brandenburg A. Hysteresis between distinct modes of turbulent dynamos // Astrophys. J. 2015. V. 803. P. 95.

Kichatinov L.L., Nepomnyashchikh A.A. Parameter modulation of dynamo waves (in Russian) // Lett. Astrophys. J. 2015. V. 41. P. 409.

1.1.12. New knowledge about properties of non-thermal electrons generated during solar flares

We obtained new knowledge about properties of non-thermal electrons generated during solar flares. Hard X and gamma radiation in 0.04-150 MeV associated with October 29, 2003 (X10 / 3B) flare was observed at 20:38–20:58 UT, using the SONG spectrometer onboard CORONAS-F. Comparison of energy spectra plotted from SONG and RHESSI data showed their proximity in a range of 0.1–10 MeV. We singled out two stages in spectra development: 20:38:00–20:44:20 UT and 20:44:20–20:58:00 UT. The efficiency of proton acceleration increased relative to acceleration of high energy electrons during the second stage. In particular, pion decay is statistically significant only in the second phase of the flare. The power proton index is 3.7 relative to pion and gamma lines. The changes in acceleration characteristics agree with synchronous changes in a spatial structure of the flare. The flare is associated with GLE 66. We found that the GLE onset agrees with pion line appearance.

Publications:

Kurt V.G., Yushkov B.Yu., Kudela K., Galkin V.I., Kashapova L.K. CORONAS-F observation of HXR and gamma-ray emissions from the solar flare X10 on 29 October 2003 as a probe of accelerated proton spectrum // Contributions of the Astronomical Observatory SkalnatéPleso. 2015. V. 45. Pp. 42–59.

1.1.13. Height stratification of a spatial distribution of intensity of low frequency oscillations in active regions

We determined the height stratification of a spatial distribution of intensity of low frequency oscillations (0.7–2 mHz) of the radial velocity and intensity in active regions. We developed a seismological method for measurement of the

height and average sound velocity between the layers of the atmosphere of sunspot umbrae observed at different wavelengths. The proposed method allows us to estimate these values without additional assumptions about sound velocity or heights of emission generation. After using this method, we estimated a distance between emitting layers in temperature minimum (1600 Å) and transition zone (304 Å) above sunspot umbra in three active regions, namely, NOAA 11131, 11582, 11711. We also estimated average sound velocity. Average distance between temperature minimum and transition zone was around 500–800 km, and corresponding average sound velocity was 30 km/s, which was close to average sound velocity in the solar atmosphere.

Publications:

Deres A.S., Anfinogentov S.A. Measurement of the formation heights of UV and EUV emission above sunspot umbrae from observations of three-minute oscillation // *Astronomy Reports*. 2015. V. 59. Pp. 959–967.

1.1.14. Multi-wave measurements of characteristics of propagating oscillations

We carried out multi-wave measurements of characteristics of propagating oscillations. Research of spatial structure of 3-minute oscillations in sunspots revealed that they were propagating into the ambient atmosphere through channels, magnetic flux tubes. It turned out that such channels could have been connected with the regions where the solar flares initiated. For this study, we selected June 7, 2012 flare with a maximum at 05:56 UT and C1.5 intensity before which correlation curves from Nobeyama Radio Heliograph had shown oscillations with a period of around 3 minutes. The oscillations of correlation curves reflect changes in structure and intensity of compact radiation sources at 17 GHz. We discovered that amplitude of oscillations had been increasing for 30

min before the flare. The space-time distributions of wave amplitude in radio and ultraviolet emission (SDO/AIA of 94 and 171 Å) were received, using pixel wavelet filtration. It was shown that 3-minute oscillations were generated in a sunspot and propagated in chosen directions, i.e., magnetic channels. This stage revealed transverse oscillations of the flare loop with a period of around 30 seconds (in sequences of images at 17 GHz). The height cuts of space localization of frequency modes in active regions allow us to trace the wave disturbance path (Fig. 12).

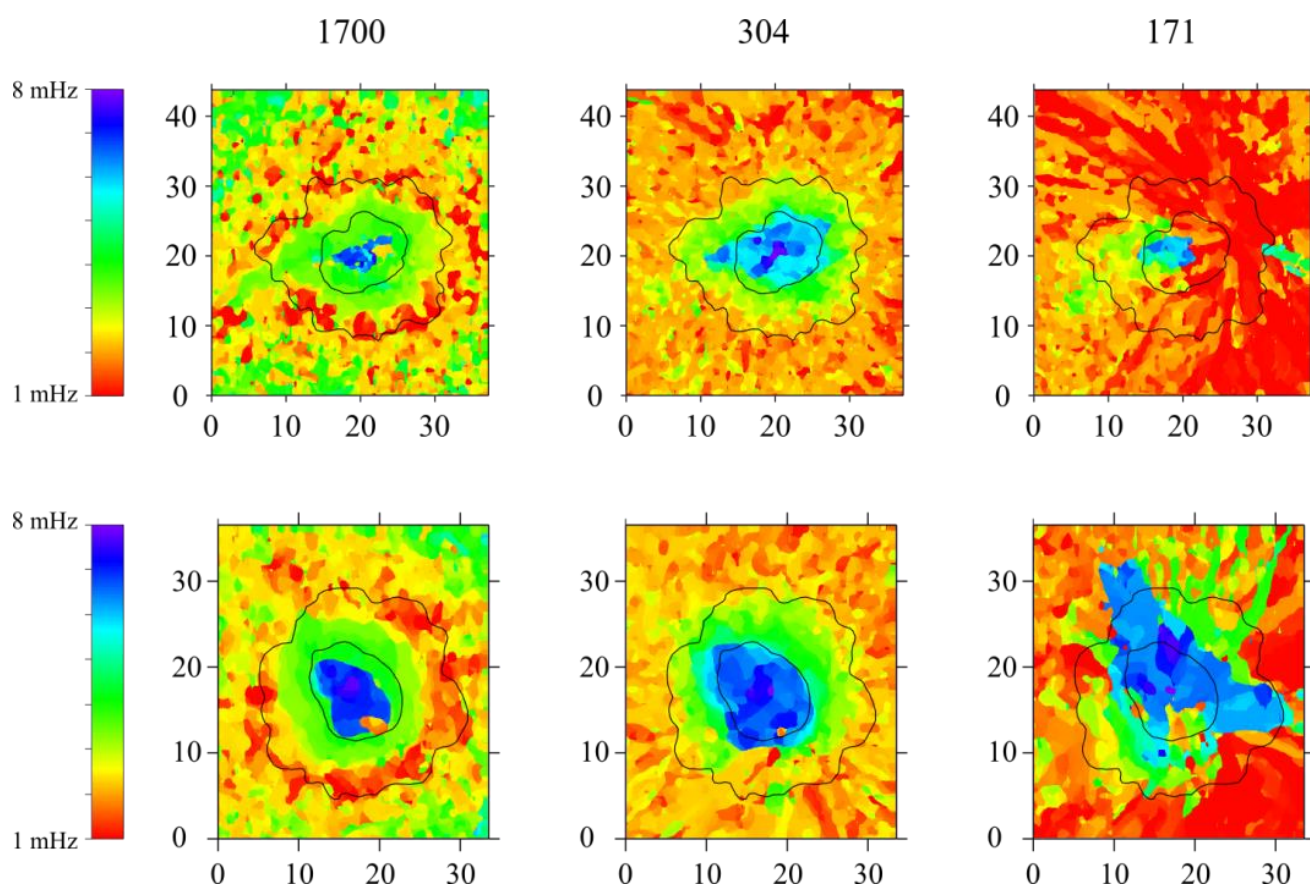


Fig. 12. The spatial location of the oscillation of two sunspots at wavelength 1700, 304, 171 Å. X, Y axes use arcseconds, the color corresponds to the oscillation frequency.

Publications:

Sych R., Karlický M., Altyntsev A., Dudík J., Kashapova L. Sunspot waves and flare energy release // *Astronomy & Astrophysics*. 2015. V. 577. Id. A43, P. 8.

Sych R. Waves and oscillations in the sunspot atmosphere: an overview (in Russian) // Solar-terrestrial physics. 2015. V. 1, N. 2. Pp. 3–21.

1.1.15. Characteristics of inhomogeneities in solar wind fluxes at distances from 3 to 15 solar radii from STEREO data

We studied characteristics of inhomogeneities in solar wind fluxes at distances from 3 to 15 solar radii from STEREO data. We defined such parameters of inhomogeneities as form, sizes, time of formation, change in velocity and acceleration (Fig. 13). We compare the received values for polar and low-latitude regions of the solar corona. It was discovered that SW fluxes underwent significant changes in velocity with accelerations of both signs in polar and low-latitude regions of the solar corona, which could have been explained by presence of MHD forces affecting SW fluxes and by turbulence generation at flux fronts. We studied sources of inhomogeneities and possible regions of their formation from AIA/SDO and EUVI/STEREO data.

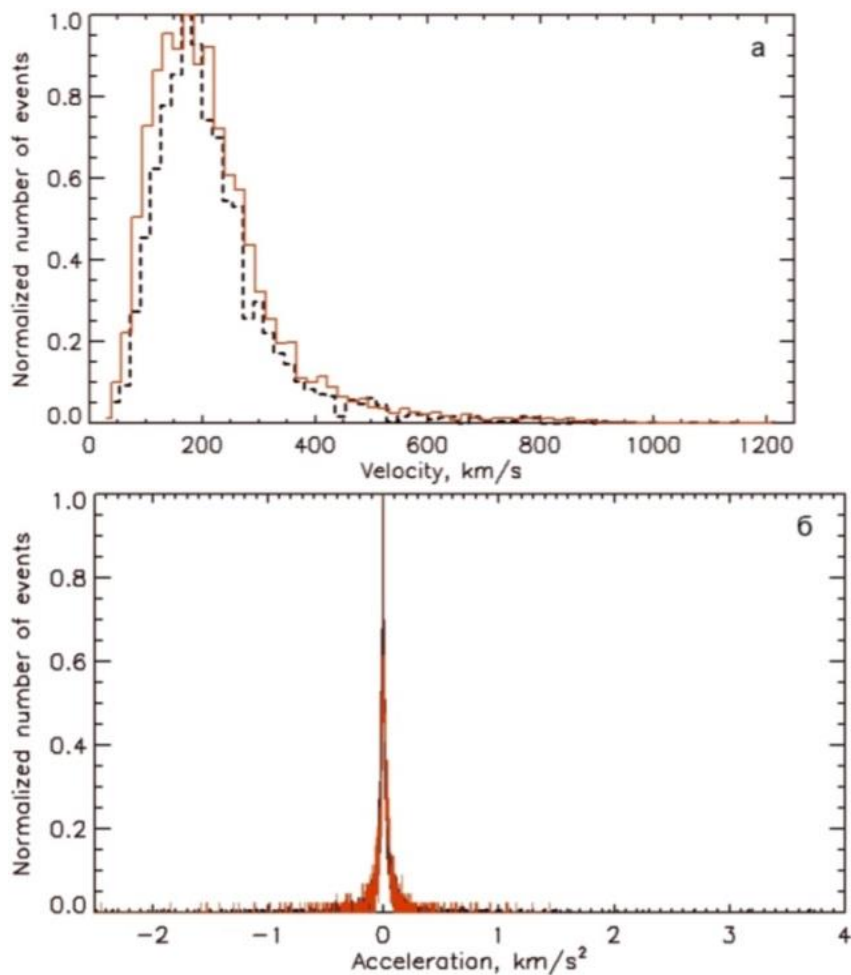


Fig. 13. The velocity (top) and acceleration (bottom) normalized histograms of the solar wind at polar and low-latitude regions of the Sun. Results for polar regions are marked by red color; for low-latitude ones, by black color.

Publications:

Kudryavtseva A.V., Prosovetsky D.V. Sources of small scale inhomogeneities of solar wind and dynamic parameters of solar wind flux in the outer solar corona (in Russian) // Baikal Young Scientists' International School on Fundamental Physics. Proc. The XIVth Conference of Young Scientists "Interaction of Fields and Radiation with Matter", Irkutsk, 2015. Pp. 33–35.

1.1.16. Changes in the field of an active region accompanying by coronal mass ejection (CME) on June 7, 2011 associated with filament eruption and solar flare

Vector photospheric magnetic field measurements by SDO/HMI were used to study variations in the solar magnetic field in an active region accompanying emergence of the June 7, 2011 CME associated with filament eruption and solar flare. We analyzed variations in the absolute value of the magnetic induction vector B , radial field component B_r , as well as in an angle α between the magnetic field direction and radial direction from the solar center. We established that the event was preceded with surfacing of a new magnetic flux (NMF) in several zones. In one zone, the polarity in the vicinity of eruptive filament, NMP was of a small spot, a pore, whose polarity and amplitude were favorable to magnetic field line reconnection with the ambient field. We studied variations in angles α before and after the onset of the event in different parts of the active region where the considered event had occurred. We revealed that the angle α decreased with different rate during several hours before the onset of the event in several zones under consideration. In the flare region in the vicinity of the neutral line of the magnetic field, we observed a sharp increase in the transverse component of the magnetic field and approximately 25–30% increase in inclination angle to the radial direction after the onset of the event. This effect predicted by a number of researchers was discovered for the first time.

Publications:

Fainshtein V.G., Egorov Ya.I., Rudenko G.V., Anfinogentov S.A. Variations in the magnetic field in an active region accompanying by CME associated with filament eruption // The proceedings of the XIXth Annual All-russian Conference on Solar Physics "Solar Physics 2015", 2015 Solar and Solar-Terrestrial Physics (October 5–9, 2015, the GAO RAS, Saint-Petersburg), Pp. 359–362.

1.1.17. Role of solar filament in generation of a flare, CME, and shock wave

We showed the role of solar filament in generation of a flare, CME, and shock wave. We proposed an updated scenario of an eruptive flare, coronal mass ejection (CME), and evolution of a shock wave. Initial destabilization of filament leads to extension of magnetic threads belonging to its body and rooted in the photosphere along the inversion line. Their reconnection result in:

- 1) heating of filament parts or its environment;
- 2) initial formation of a flare loop cusp, arcade, and ribbons;
- 3) rising similarity between filament and magnetic flux rope;
- 4) to its acceleration.

Then the pre-eruptive arcade encompassing filament is involved in reconnection in accordance with a standard model, continuing the formation of a flare arcade and ribbons. The poloidal magnetic field in a curved flux rope forming from filament steadily increases, facilitating its toroidal extension. The magnetic flux rope impulsively extends, exciting magnetohydrodynamic disturbance which rapidly steepens into a shock wave (Fig. 14). The wave passes through the arcade widening above filament and then during some time runs in front of CME like a slowing blast wave (Fig. 15). If CME is slow, the shock wave damps over time. Otherwise, the shock front turns into a piston mode. We found that reconnection in a current layer of a remote streamer caused by passage of the shock front excites in a streamer a running process similar to a flare which was responsible for radio emission of the second type.

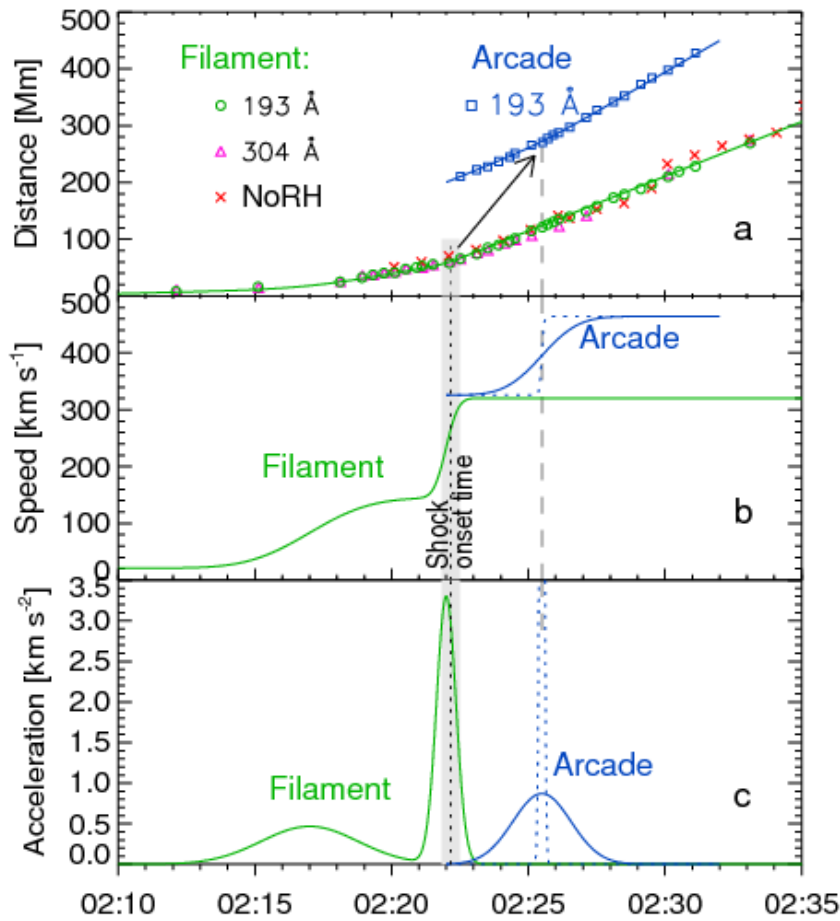


Fig. 14. The eruptive event on May 11, 2011. Kinematics of an eruptive filament and arcades above it and generation of a wave. a. Distance from the photosphere. b. Lift-off speed. c. Acceleration. Time of a shock wave formation is marked with the vertical lines.

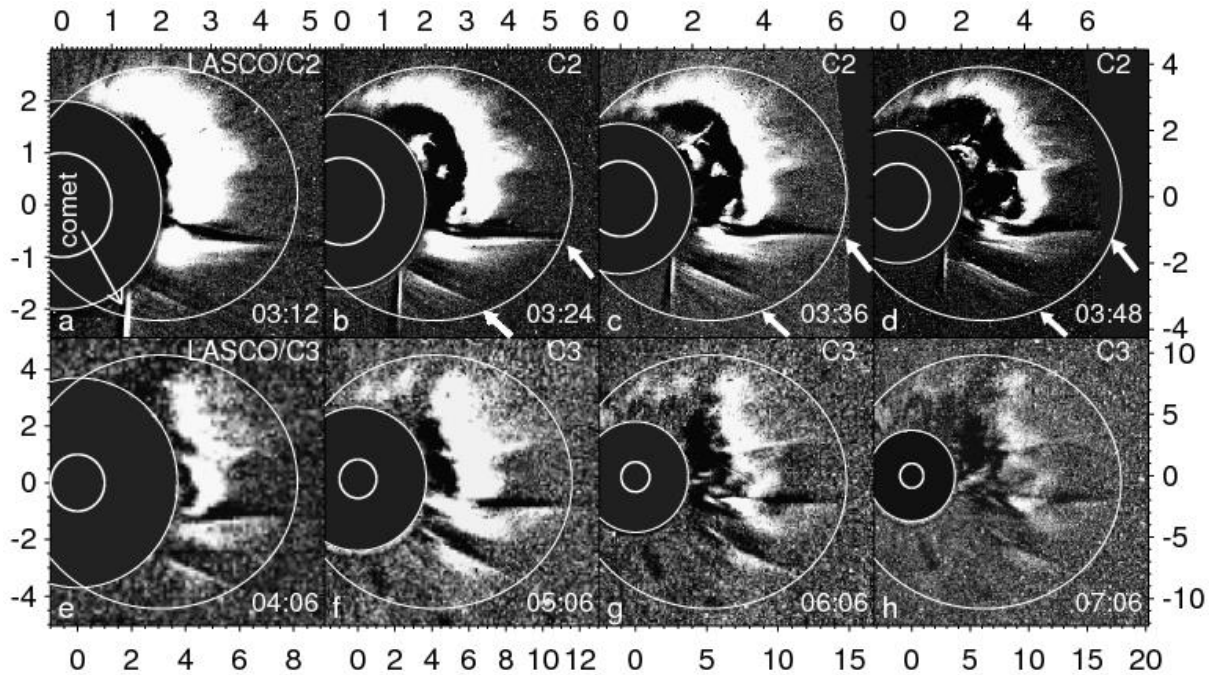


Fig. 15. The trace before the CME on May 11, 2011 event. The ellipses represent the calculated fronts of a decelerating wave. All the images are resized to keep the expanding wave front fixed.

Publications:

Grechnev V.V., Uralov A.M., Kuzmenko I.V., Kochanov A.A., Chertok I.M., Kalashnikov S.S. Responsibility of a filament eruption for the initiation of a flare, CME, and blast wave, and its possible transformation into a bow shock // Solar Physics. 2015. V. 290. Pp. 129–158.

1.1.18. Estimation of an X-ray magnitude of post-limb flare observed by STEREO/EUVI

The IZMIRAN together with the ISTP SB RAS proposed a simple method for estimation of an X-ray magnitude of post-limb flare observed by STEREO/EUVI. Blooming effects shown as almost horizontal stripes aside brightest flare sources are observed near a maximum of significant solar flares in images from STEREO/EUVI 195 Å (Fig. 16). We found that the length of these blooming streaks could have been used to estimate soft X-ray flux and X-ray magnitude of post-limb flares registered on one of the two STEREO spacecrafts, invisible from the Earth. For this purpose, we established an empirical correlation $F_G = 392 \pi (L/R_S)^{1.42}$ between a peak GOES flux in the range 1–8 Å F_G and relative length of an blooming streak L/R_S (Fig. 17) from the the data on approximately 350 flares observed from January 2007 to July 2014 (most of which exceeded M1.0 level).

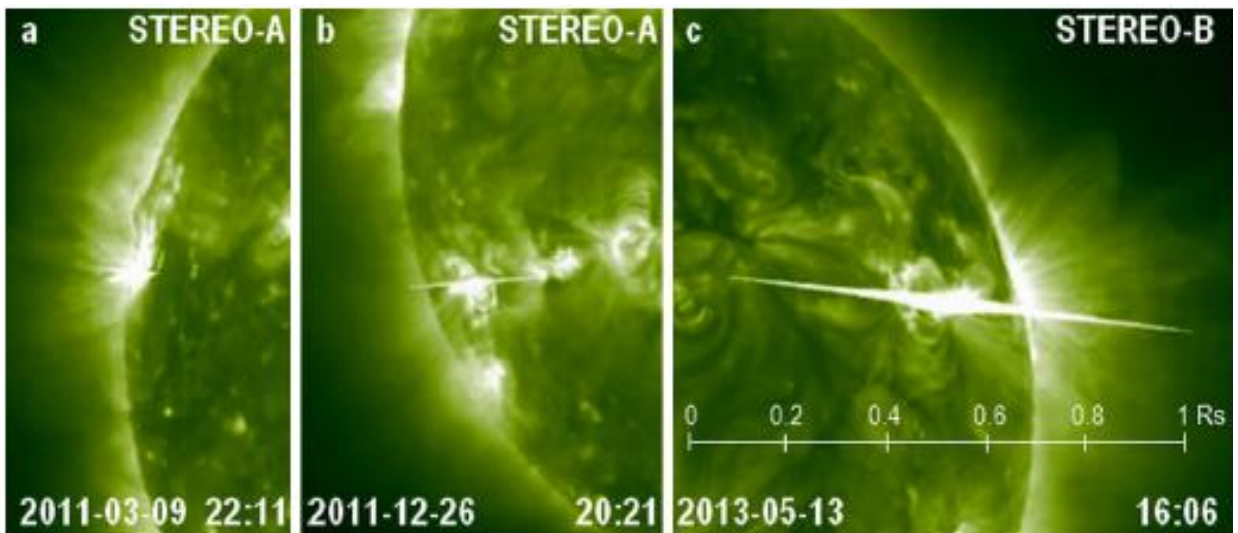


Fig. 16. The STEREO/EUVI 195 Å images with blooming streaks typical of C (a), M (b), and X (c) class flares. The spatial scale shown in panel (c) is the same for all of the three images.

This method allowed us to estimate X-ray magnitudes of approximately 65 energetic post-limb flares observed by STEREO during the same years. The results of this simple and operative method agree with estimates based on calculation of a response of EUVI telescopes from the entire solar disk. In addition, we studied some peculiarities of blooming streaks in impulse and long flares. It was shown that these bars in consecutive EUVI images could have been used for reconstruction of a possible history of energetic post-limb flare.

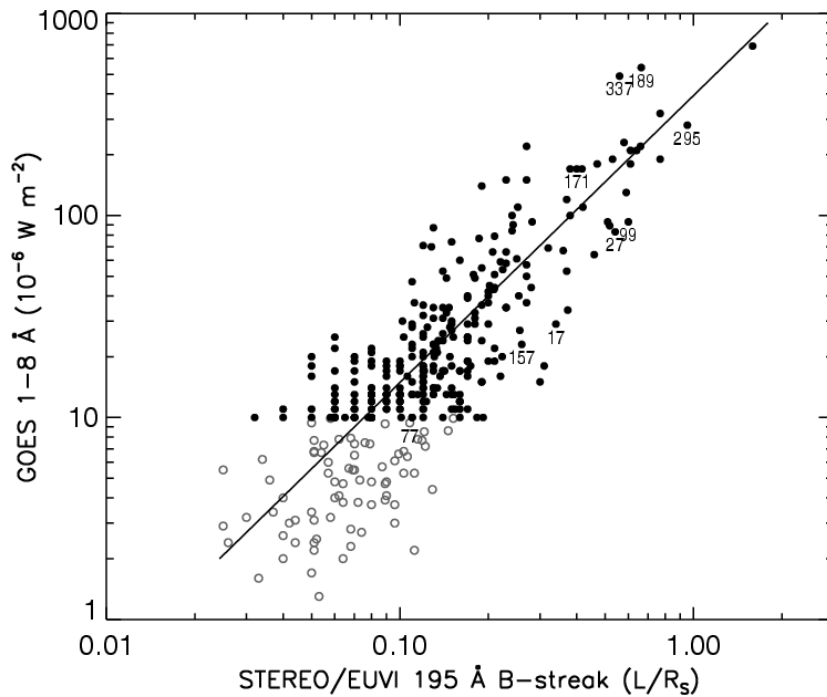


Fig. 17. The relation between the relative lengths of the STEREO/EUVI 195 Å blooming streaks versus the GOES 1–8 Å fluxes. The gray open circles denote C-class flares; the black filled circles, \geq M1-class flares.

Publications:

Chertok I.M., Belov A.V., Grechnev V.V. A Simple Way to Estimate the Soft X-ray Class of Far-Side Solar Flares Observed with STEREO/EUVI // *Solar Physics*. V. 290. Pp. 947–1961.

1.1.19. Relation between magnetic flux involved in solar eruptions and Ap-index during geomagnetic storms

The IZMIRAN together with the ISTP SB RAS determined the relation between magnetic flux involved in solar eruptions and Ap-index during geomagnetic storms. The coronal mass ejections (CMEs) are the main sources of the most powerful non-recurrent geomagnetic storms. In the extreme ultraviolet, CMEs are accompanied by bright post-eruptive arcades and dark dimmings. Analysis of events of the 23rd solar cycle showed that the total unsigned magnetic flux Φ in arcades and dimmings at the photospheric level was significantly

associated with intensity of geomagnetic storms described by D_{st} -index. This fact provides basis for earlier detection of geoefficiency of solar eruptions. The same data set showed presence of a significant correlation between eruptive magnetic flux Φ and A_p geomagnetic index (Fig. 18).

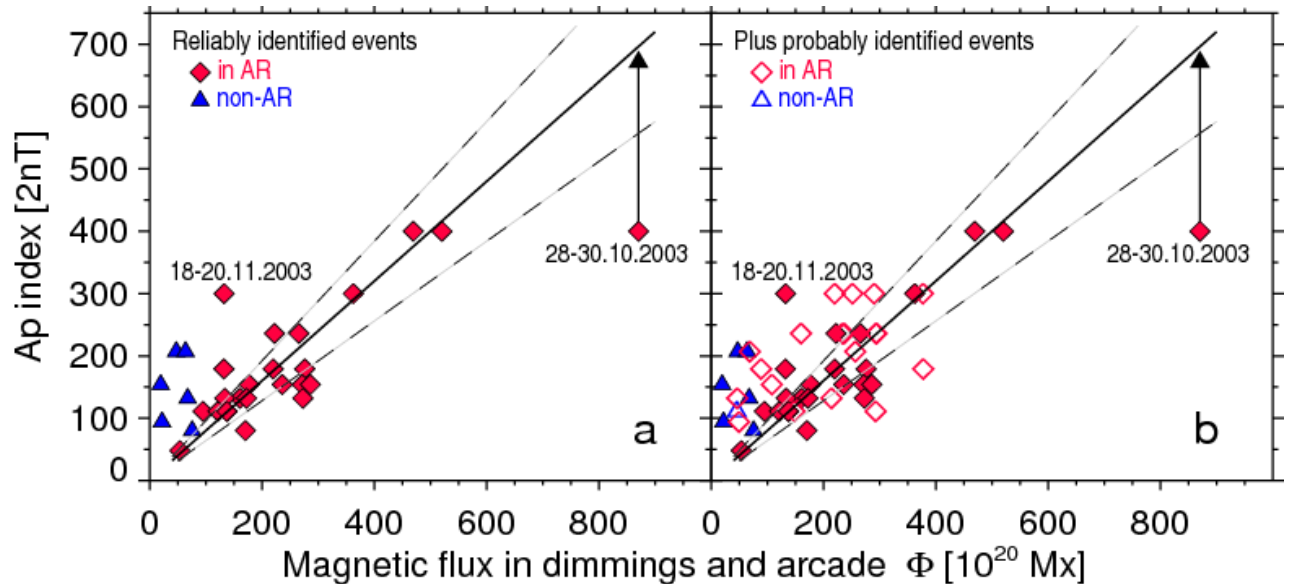


Fig. 18. The dependence of the geomagnetic A_p index on the total magnetic flux in the arcades and dimming regions: (a) for geomagnetic storms with reliably identified solar eruptions, (b) events with probable identification (open symbols)..

With increasing magnetic flux from several dozens to ≈ 500 (in 10^{20} Mx), intensity of a geomagnetic storm measured by three-hour A_p index increases in an average of $A_p \approx 50$ up to a formal upper limit of 400 (in 2 nT). The defined correlation $A_p = 0.8 \Phi$ testifies that the real value of A_p index is not limited and can significantly exceed 400 during the strongest magnetic storms.

Publications:

Chertok I.M., Abunina M.A., Abunin A.A., Belov A.V., Grechnev V.V. Relationship between the magnetic flux of solar eruptions and the A_p index of geomagnetic storms // Solar Physics. 2015. V. 290. Pp. 627–633.

1.1.20. Nonlinear effects in propagation of slow magnetosonic waves in coronal plasma structures

We discussed nonlinear effects in propagation of slow magnetosonic waves in coronal plasma structures. Dynamics of observed longitudinal waves in coronal plume structures was theoretically considered with respect to dissipation, nonlinearity, magnetic nature of waves, and waveguide nature of their propagation. We derived Burgers evolution equation describing propagation of weak nonlinear slow magnetosonic waves in homogeneous thin magnetoplasma tubes. We obtained delayed generation of shock fronts in a profile of a tube wave, as well as more intensive attenuation of a tube wave in comparison to sound waves. Both effects received are significant for $\beta \sim 1$ and $\beta > 1$. On the contrary, for $\beta \ll 1$ evolution of the tube wave slightly differs from evolution of sound waves (Fig. 19).

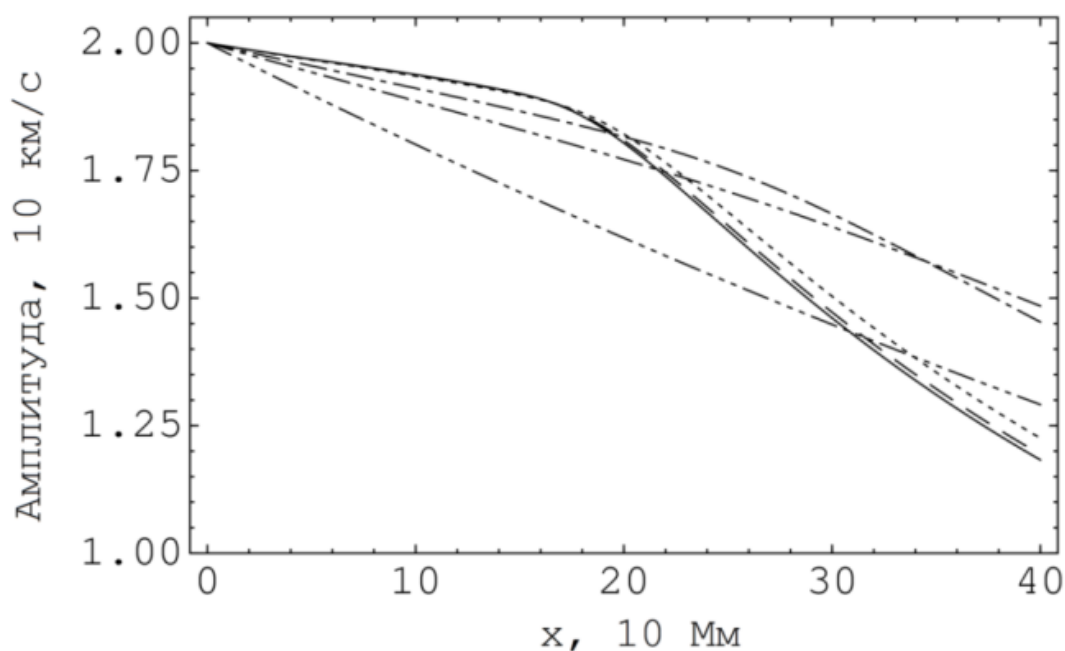


Fig. 19. The tube wave magnitude dependence versus plasma parameter β . The dotted, stroke, dash-and-dot, 2nd dash-and-dot and 3rd dash-and-dot lines correspond to values of Alfvén velocity of 866, 433, 130, 87 and 43 km/s, with sound velocity of 175 km/s in the solar corona. The value of kinematic viscosity is $2.4 \times 10^{14} \text{ cm}^2/\text{s}$. The solid line corresponds to a case of an infinitely strong magnetic field, i.e., ordinary sound waves.

Therefore, models developed for weak nonlinear sound waves can be used for analysis of longitudinal waves at the bottom of coronal plumes and magnetic fan structures with plasma temperature of ~ 1 MK. But the effects received are important for analysis of evolution of longitudinal waves in hot flare loops, magnetic fan structures filled with hot dense plasma (> 6 MK), coronal plumes with $\beta \sim 1$ (higher in the solar corona).

Publications:

Afanasyev A.N., Nakariakov V.M. Nonlinear slow magnetoacoustic waves in coronal plasma structures // *Astronomy & Astrophysics*. 2015. V. 573. P. A32.

1.1.21. Effect of magnetic nature of longitudinal waves in coronal plasma tubes and waveguide nature of their propagation

It was shown that magnetic nature of longitudinal waves in coronal plasma tubes and waveguide nature of their propagation led to a significant decrease

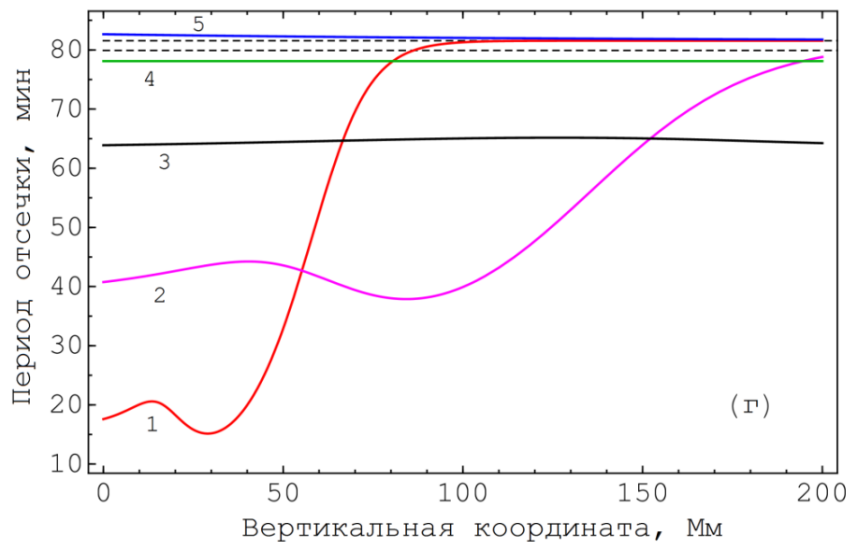


Fig. 20. The longitudinal wave cutoff period versus height for the exponentially diverging magnetic tube with plasma $\beta \ll 1$. The different curves correspond to the different typical scales L of the dependence magnetic field versus height with respect to the barometric scale of the plasma density H . For the curve 1, $L=0.2 H$; 2, $L=0.5 H$; 3, $L=H$; 4, $L=2H$; 5, $L=5H$. The dashed lines show the values of acoustic cutoff period (bottom) and Brunt-Väisälä period (top).

in values of a period of cutoff of the waves in comparison to models of sound waves and tube waves in an approximation of constant Alfvén velocity in a tube.

Reduction of the cutoff period of the waves in strongly diverging cold plasma tubes can limit a flux of waves with periods greater than that of cutoff, as well as can be responsible for generation of coronal oscillations of respective periods during pulse excitation of coronal plasma (Fig. 20).

Publications:

Afanasyev A.N., Nakariakov V.M. Cutoff period for slow magnetoacoustic waves in coronal plasma structures // *Astronomy & Astrophysics*. 2015. V. 582. P. A57.

1.2. Optical research

1.2.1. National network of the Solar Telescopes for Operational Predictions (STOPs) of the new generation has been put into experimental operation

Three STOP telescopes are developed and produced by the ISTP SB RAS and Institute of Automation and Electrometry, SB RAS and installed at three observatories in Russia (Ussuriysk, Irkutsk, Kislovodsk). The telescopes are intended for receipt of daily data on large-scale magnetic fields on the solar disk (Fig. 21). Informativeness and accuracy of measurements of magnetic field intensity are the best for similar systems in the world. The first regular observations allowed us to record polarity reverse of the solar magnetic field completed in September 2014 showed good possibilities of forecasting based on magnetograms of parameters of interplanetary medium, in particular, solar wind velocity.

The telescopes are part of the reconstructed national Solar Patrol intended for continuous observation and analysis of solar activity, space weather forecasting, and evaluation of solar activity effects on solar-terrestrial relations. This will allow us to carry out regular comprehensive observations of solar activity at all the heights of the solar atmosphere from the photosphere to the solar corona. Data from the network of the national Solar Patrol are critically important for outer space exploration, navigation systems, distant and mobile radio communication, safety of distributed technology systems and other technologies.

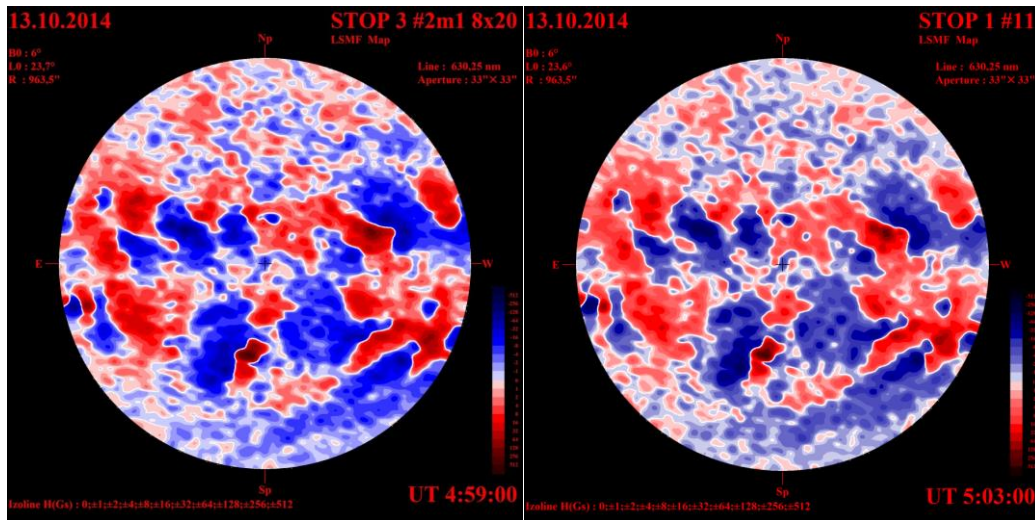


Fig. 21. The example of October 13, 2014 solar magnetic fields maps, measured almost simultaneously. The left panel shows magnetogram obtained in Kislovodsk at the Mountain Astronomical Station of the Main Astronomical Observatory (MAS MAO RAN); the right panel, magnetogram, obtained at the Baikal Astrophysical Observatory (BAO ISTP).

Publications:

Tlatov A.G., Dormidontov D.V., Kirpichev R.V., Pashchenko M.P., Shramko A.D., Peshcherov V.S., Grigoryev V.M., Demidov M.L., Svidskii, P.M. Study of some characteristics of large-scale solar magnetic fields during the global field polarity reversal according to observations at the telescope-magnetograph Kislovodsk Observatory // *Geomagnetism and Aeronomy*, 2015. V.55, № 7, P. 969-975.

Tlatov A.G., Pashchenko M.P., Ponyavin D.I., Svidsky P.M., Peshcherov V.S., Demidov M.L. Prediction of solar wind parameters from STOP magnetograph data (in Russian) // *Geomagnetism and Aeronomy*. 2016. V. 56, N. 8.

1.2.2. Experimental operation of AZT-33VM wide-angle telescope, a new unique instrument

At the Sayansk Solar Observatory of the ISTP SB RAS, we put into experimental operation the Russia's first ever AZT-33VM wide-angle telescope for fast sky survey with high penetrability to find fundamental solutions of the

structure of the Universe, near-Earth space monitoring, information about groupings of spacecrafts, space debris, and asteroid and comet impact hazards.

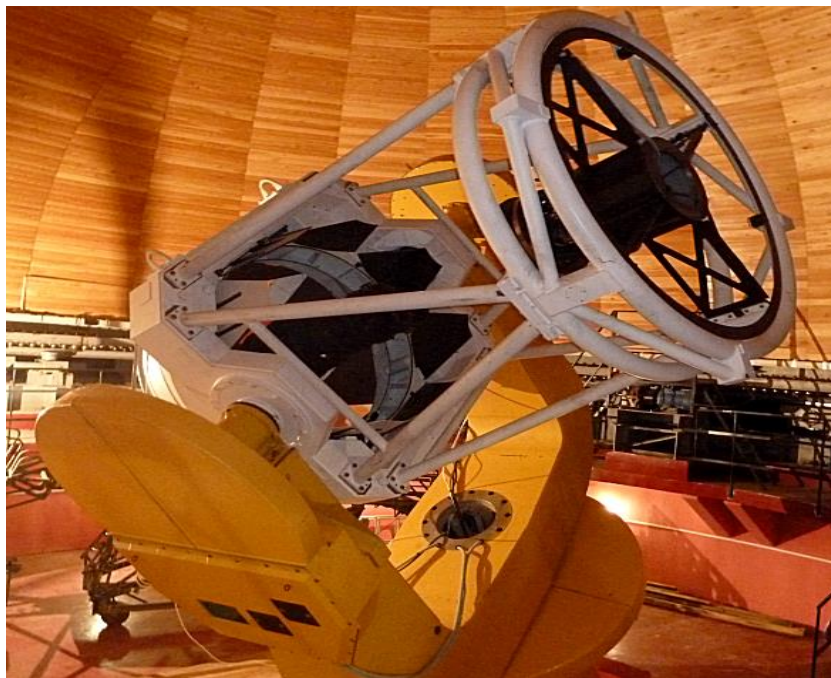


Fig. 22. The top panel shows the main view of the Astrophysical Observation Complex of the Sayansk Solar Observatory. On the left, you can see the AZT-33 IK telescope tower; on the right, the AZT-33 VM telescope tower. A technical building with a telescope control center is located between them. The bottom panel depicts the newly mounted AZT-33 VM telescope put into operation at the end of the year 2015. The diameter of the main telescope mirror is 1.6 m; focal distance, 5.6 m; field of view, 3x3 degrees.

After putting the AZT-33VM telescope into operation at the Sayansk Solar Observatory, we created a unique Astrophysical Complex consisting of two telescopes close in parameters (AZT-ZZIK infrared telescope was put into operation several years earlier), allowing us to resolve important theoretical and applied problems (Fig. 22). In particular, from both telescopes we performed test observations of a spacecraft in the vicinity of the libration point L1 in the Sun–

Earth system during 2014-2015. We selected Gaia spacecraft as an object of observation (Satellite Catalog Number No. 39479, distance from the spacecraft to the observation station of 1.5 million km). Visible luminosity has not exceeded 20.7 stellar magnitude during all the observation time, changed in the range from 20.7 to 22 stellar magnitude.

Publications:

Korobtsev I.V., Goryashin V. Ye., Eselevich M.V., Results of spacecraft tracking in the vicinity of the libration point L1 in the Sun–Earth system (in Russian) // *Astronomical journal*, 2016 (in print).

Kiehlmann S., Savolainen T., Jorstad S. G., Sokolovsky K. V., Schinzel F. K., Marscher A. P., Larionov V. M., Agudo I., Akitaya H., Benítez E., Berdyugin A., Blinov D. A., Bochkarev N. G., Borman G. A., Burenkov A. N., Casadio C., Doroshenko V. T., Efimova N. V., Fukazawa Y., Gómez J. L., Grishina T. S., Hagen-Thorn V. A., Heidt J., Hiriart D., Itoh R., Joshi M., Kawabata K. S., Kimeridze G. N., Kopatskaya E. N., Korobtsev I. V., Krajci T., Kurtanidze O. M., Kurtanidze S. O., Larionova E. G., Larionova L. V., Lindfors E., López J. M., McHardy I. M., Molina S. N., Moritani Y., Morozova D. A., Nazarov S. V., Nikolashvili M. G., Nilsson K., Pulatova N. G., Reinthal R., Sadun A., Sasada M., Savchenko S. S., Sergeev S. G., Sigua L. A., Smith P. S., Sorcia M., Spiridonova O. I., Takaki K., Takalo L. O., Taylor B., Troitsky I. S., Uemura M., Ugolkova L. S., Ui T., Yoshida M., Zensus J. A., Zhdanova V. E. Polarization angle swings in blazars: The case of 3C 279 // *Astronomy & Astrophysics*. 2016. V. 590. id. A10. Pp. 1-20. DOI: 10.1051/0004-6361/201527725.

1.2.3. Revealed inversion of the solar polar magnetic fields in the current solar cycle

We established that the cause of asynchrony in inversion of the solar polar magnetic fields was associated with northerly-southern asymmetry of its magnetic activity (Fig. 23 *a, b*). Latitude-time analysis shows an increase in activity in the cycle and inversion of the solar polar magnetic fields (Fig. 23, *b*). The unipolar magnetic regions (UMRs) of following polarities form after decay of active regions with positive inclination angles to the equator (the leading sunspots are closer to the equator than preceding ones). Analysis showed that UMRs of the leading polarities raised after decay of groups of sunspots with negative inclination angles to the solar equator.

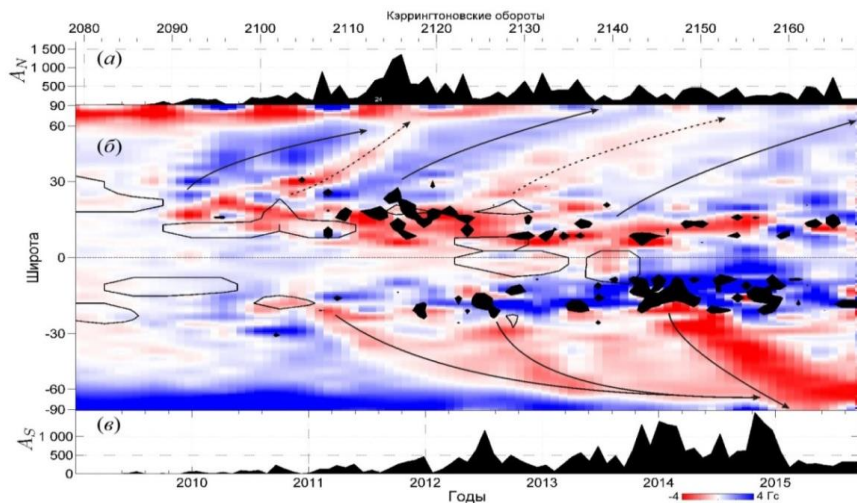


Fig. 23. The changes in areas of sunspots in the Northern (a) and Southern Hemispheres of the Sun, (b) the latitudinal-time diagram of the photospheric magnetic fields (blue and red colors) and a region of spot formation (black filling). The solid and dotted arrows indicate UMRs of preceding and leading polarities. The regions where the negative inclination angles of groups of sunspots predominate are shown by the contours.

Publications:

Mordvinov A.V., Grigoryev V.M., Erofeev D.V. Evolution of sunspot activity and inversion of the Sun’s polar magnetic field in the current cycle // Advances in Space Research 2015. V. 55. P. 2739.

2. Physics of near-Earth cosmic space

2.1. Magnetospheric research

2.1.1. Experimental confirmation of existence of small-scale transverse waves Alfvén waves with spatially dependent polarization in Earth's magnetosphere

For the first time, using the data from the satellites of Van Allen Probes mission (RBSP-A), we managed to detect monochromatic Alfvén waves with complex polarization depending on the position of their magnetic shell. A theoretical work predicted the waves with such a polarization more than twenty years ago for the first time. At that time, there were no spacecrafts for observation of such oscillations. Only now, we have multi-satellite systems capable of observing magnetospheric oscillations with high spatial resolution.

As theory suggests, these oscillations in the region of their generation are poloidal standing Alfvén waves. The oscillations of plasma and magnetic field in these waves occur in the plane of the magnetic meridian. The poloidal Alfvén waves run away from the region of their generation across the magnetic shells, remaining standing waves along the magnetic field lines. At a greater distance from the region of their generation, the standing Alfvén waves gradually transform from poloidal into toroidal ones. In toroidal Alfvén waves, oscillations of plasma and magnetic field are perpendicular to the plane of the magnetic meridian (and, therefore, perpendicular to the direction of oscillations in their generation region) (Fig. 24, on the left). At resonance magnetic shell, the toroidal Alfvén waves are completely absorbed because of their dispersion in the conducting layer of the ionosphere.

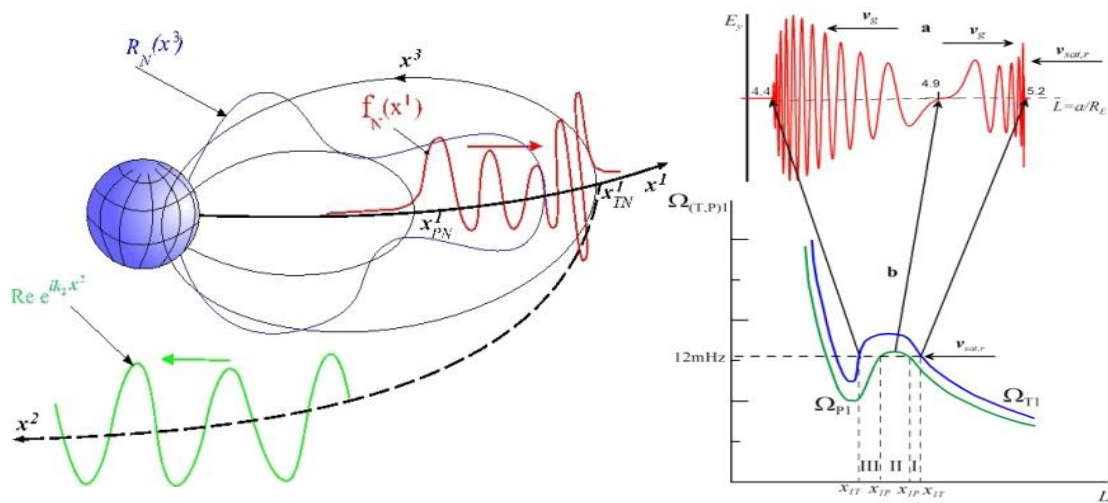


Fig. 24. (left): The theoretically predicted structure of a monochromatic azimuthally small-scale Alfvén wave in a dipole magnetosphere.

(right): (a) Structure of the Alfvén-like oscillation registered by RBSP-A spacecraft while crossing the plasmopause on October 23, 2012, (b) their binding to the structure of eigenfrequencies of the fundamental harmonics of poloidal (Ω_{p1}) and toroidal (Ω_{T1}) standing Alfvén waves (L is a magnetic shell parameter).

It is such oscillations that were registered for the first time by the RBSP-A satellite. Based on structure of the recorded oscillations, we concluded that the satellite crossed two regions of existence of such oscillations located close to the plasmopause (Fig. 24 (on the right), panels (a) and (b)). A satellite trajectory was such that it first crossed the resonance magnetic shell (outer to the plasmopause) for toroidal Alfvén waves. Here the waves had a toroidal polarization. Then the satellite dislocated to the region of oscillation generation situated on the plasmopause. At the same time, the polarization of the recorded monochromatic oscillations (with frequency about 12 mHz) continually changed from toroidal to poloidal. Then polarization of the recorded oscillations altered. As the satellite dislocated from the region of generation to an inner toroidal resonance shell, polarization of oscillations gradually changed from poloidal into toroidal one. This

fully agreed with theoretical prediction of behavior of small-scale transverse Alfvén waves, which suggested that it was the first experimental confirmation of existence of such waves in Earth's magnetosphere.

Publications:

Leonovich A.S., Klimushkin D.Yu., Mager P.N. Experimental evidence for existence of monochromatic transverse small-scale standing Alfvén waves with spatially depending polarization, *J. Geophys. Res., Space Physics*, V. 120, pp. 5443–5454, doi:10.1002/2015JA021044, 2015.

Leonovich, A. S., and V. A. Mazur (1993), A theory of transverse small-scale standing Alfvén waves in an axially symmetric magnetosphere, *Planet. Space Sci.*, 41, 697-717, doi:10.1016/0032-0633(93)90055-7.

2.1.2. Alfvén and MHD waves coupled in the geomagnetic tail

We theoretically demonstrated that a complex mode of MHD oscillations composed of Alfvén and slow magnetosonic waves forms in the field lines elongated into the tail passing through the current sheet. These waves couple with each other in the narrow current sheet of the geomagnetic tail. Along a magnetic field line, this coupled mode of oscillations is of a standing wave type between the intersection points of the field line with the ionosphere in the Northern and Southern Hemispheres (Fig. 25). Across magnetic shells, the coupled mode is of a wave propagating from the region of its generation to a resonance surface where it is fully absorbed in the ionosphere.

The fact that when the geomagnetic tail corresponds to a pre-stage of a substorm (the tail is elongated, the current sheet is thin), the coupled modes of oscillations become unstable is the most interesting feature of this mode of oscillations. This balloon instability of the coupled modes along with Tearing

instability of a current sheath is considered a cause of a substorm explosion leading to reconnection of geomagnetic field lines in the geomagnetic tail.

For the first time, we studied an entire spatial structure of coupled modes of MHD oscillations of the geomagnetic tail in the axially symmetric magnetosphere (Fig. 25), spectrum of eigenoscillation frequencies, and increments of their instability. We discovered the peculiarities of this structure which could be used for detection of these oscillations, using multi-satellite observation.

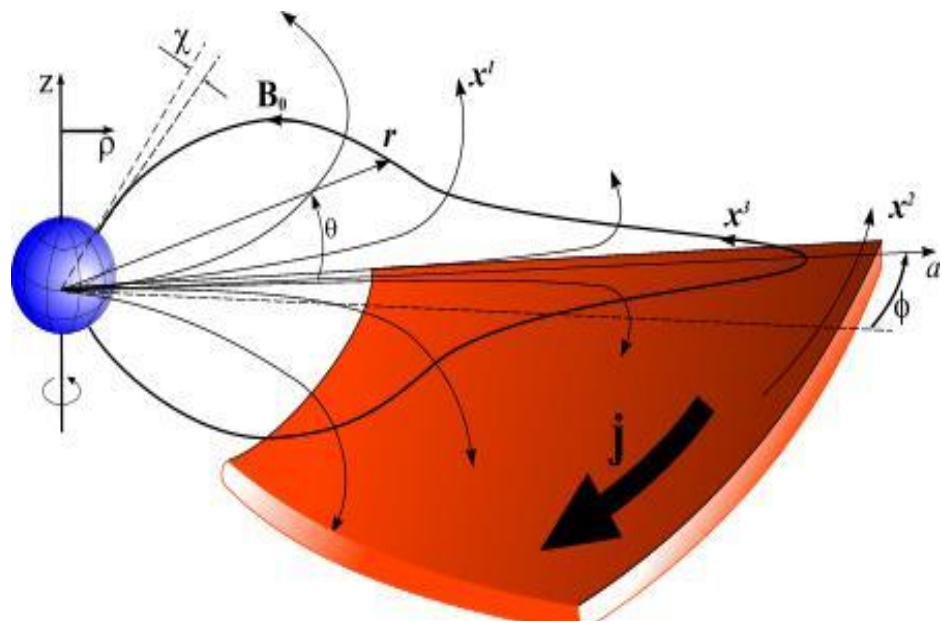


Fig. 25. An axisymmetric model of the magnetosphere with the current sheet showing: 1) the tailward stretched magnetic field lines; 2) the inclination angle of the magnetic field line to the ionosphere χ ionosphere; 3) the current sheet with current density \mathbf{j} ; 4) the coordinate systems related to the field lines: orthogonal curvilinear (x^1, x^2, x^3), cylindrical (ρ, ϕ, z), and spherical (r, θ, φ) used in the calculations.

systems. Sharp peaks must be observed in the amplitude distribution of the longitudinal component of the magnetic field of oscillations along the field line, in their inflexion points (two of which are located on two different sides close to the current sheet). Second longitudinal harmonic of the coupled waves turned out to have the greatest increment of oscillation instability.

Publications:

Leonovich, A.S. and Kozlov D.A. Coupled guided modes in the magnetotails: spatial structure and ballooning instability, *Astrophysics and Space Science*, 353, 9-23, 2014.

2.1.3. First results of the high-resolution multibeam ULF wave experiment at the Ekaterinburg SuperDARN radar: ionospheric signatures of coupled poloidal Alfvén and drift-compressional modes

Ultra low frequency (ULF) waves are frequently observed in regions of the magnetosphere with high plasma pressure where the ratio of plasma pressure to magnetic pressure exceeds unity. The nocturnal magnetosphere outside a cold plasmasphere and the geomagnetic tail are such areas. Alfvén and drift-compressional modes coupled with each other with respect to curvature of geomagnetic magnetic field lines are two most widely spread modes of oscillations in such plasma. The ample opportunities for their research are provided by SuperDARN coherent decameter radars.

Using the Ekaterinburg coherent decameter radar (built according to SuperDARN standards), we have started studying space-time characteristics of ULF waves since December 2013. Research of these waves relies on analysis of the Doppler shift of reflection of radio wave from the ionospheric F-layer. During the experiment, one of the radar channels scanned 0-2 beams, with averaged time of 6 seconds, corresponding to 18-second resolution for each beam. This allows us to detect ULF waves with periods of 40 seconds and more. Beam 0 is directed almost exactly along the magnetic meridian, thereby the recorded velocity of oscillations corresponds to the azimuthal components of the electric field.

The first examples of ULF waves of Pc5 type recorded in the course of this experiment were observed on December 14, 2013 and January 2, 2014 in the

nocturnal magnetosphere during two small magnetic storms associated with fast solar wind flux from coronal holes (Fig. 26). In both cases, the ULF waves were observed after aurora disturbances of a substorm type.

We observed two branches of oscillations with higher and lower frequencies. Frequency depended on the azimuthal wavenumber m for both branches. With increasing m , the branches verged on each other and finally fused together at a certain critical value of m^* . Such a dependence of frequency on the azimuthal wavenumber is typical for coupled Alfvén and drift-compressional modes in finite pressure plasma in the curved magnetic field as suggested a theory put forward earlier by the ISTP SB RAS (Klimushkin et al., 2012). The single branch of oscillations for $m > m^*$ is an unstable ULF mode which is a balloon drift mode (Fig. 27).

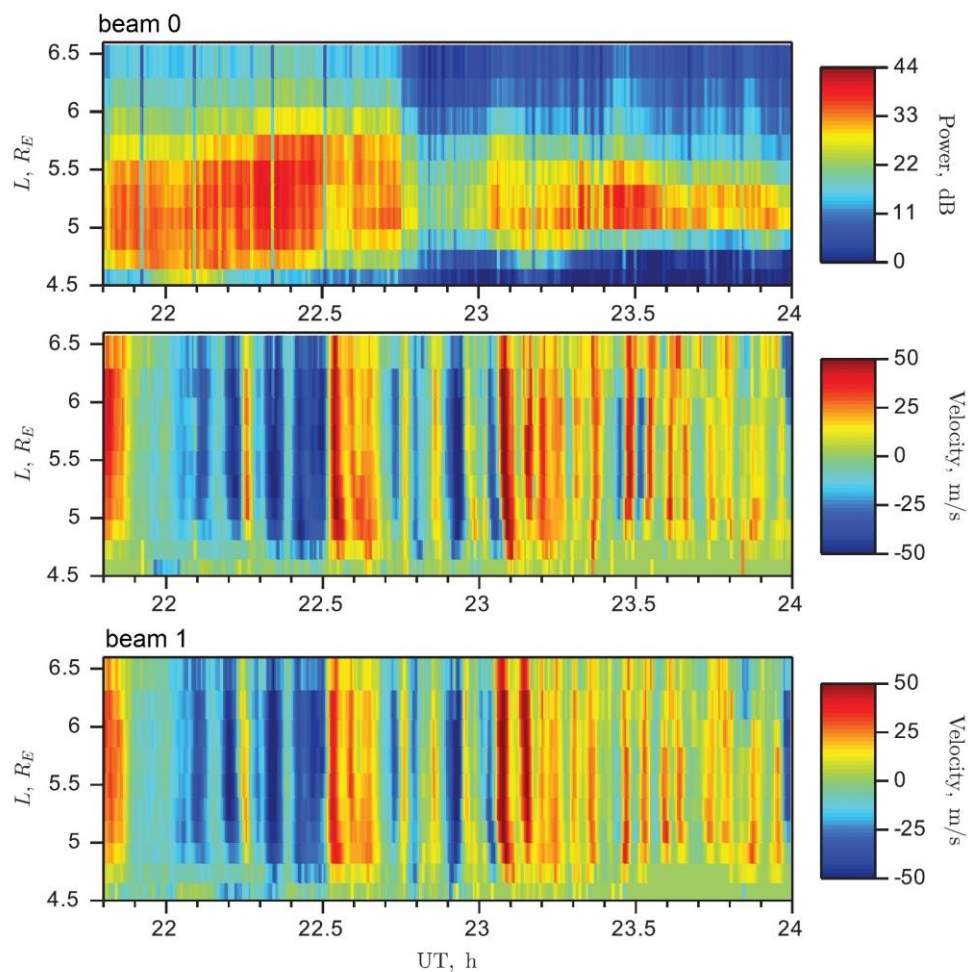


Fig. 26. December 14, 2013 ULF oscillations of plasma drift velocity registered by the Ekaterinburg radar of the Russian SuperDARN sector. The horizontal axis shows universal time;

the vertical axis, McIlwain L-parameter. From top to bottom: reflected signal power on beam 0, plasma oscillation velocity on beam 0, plasma oscillation velocity on beam 1.

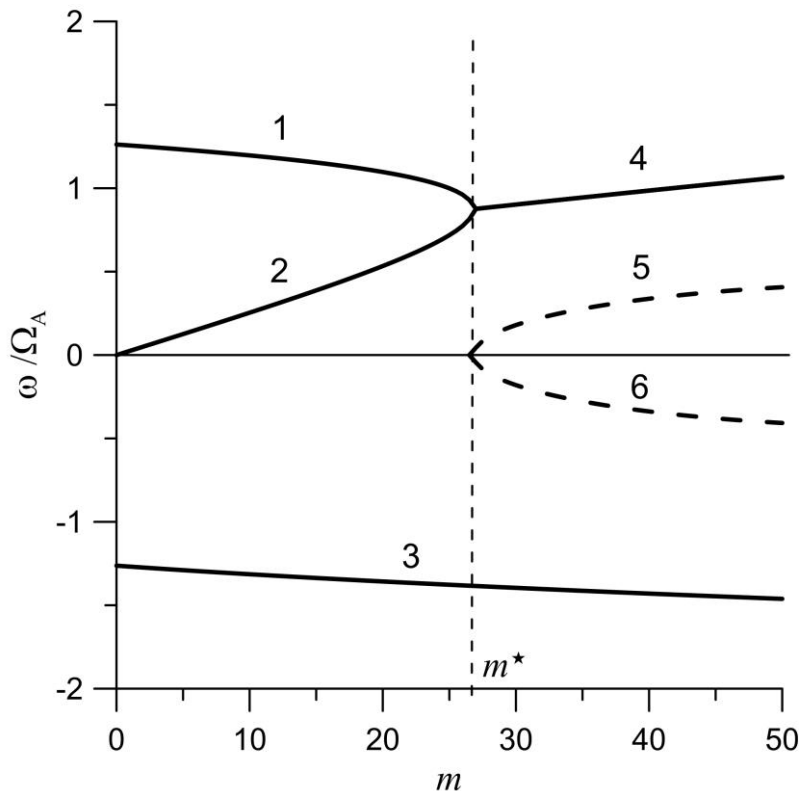


Fig. 27. The dependence of the frequency of the coupled Alfvén and drift-compressional modes in finite pressure plasma in the curved magnetic field. At $M > m^*$, the branches are coupled and the drift ballooning mode appears. Oscillation modes numbered as follows: 1 is the westerly propagating Alfvén mode; 2, the drift compressional mode; 3, the easterly propagating Alfvén mode; 4, the drift ballooning mode (real part of frequency); 5 and 6, the drift ballooning mode (imaginary part of frequency).

Thus, we suggested the following interpretation of ULF waves during our experiment with the Ekaterinburg radar: the higher frequency branch of oscillations (with precritical values of the azimuthal wavenumber $m < m^*$) was associated with Alfvén mode; the lower frequency, with a drift compressional mode; single branch at $m > m^*$, with balloon drift mode. Such a transformation of different ULF modes was not observed previously.

Publications:

Klimushkin D.Yu., Mager P.N., Pilipenko V.A., On the ballooning instability of the coupled Alfvén and drift compressional modes, *Earth, Planets, and Space*, 64, 777–781, doi:10.5047/eps.2012.04.002, 2012.

Mager P.N., Bergardt O. I., Klimushkin D.Yu., Zolotukhina N.A., Mager O.V. First results of the high-resolution multibeam ULF wave experiment at the Ekaterinburg SuperDARN radar: ionospheric signatures of coupled poloidal Alfvén and drift-compressional modes, *Journal of Atmospheric and Solar-Terrestrial Physics*, v. 130-131, p. 112-126, doi:10.1016/j.jastp.2015.05.017, 2015.

2.2. Ionospheric research**2.2.1. Generation mechanisms of large-scale and medium-scale inhomogeneities in the winter stratosphere of the Northern Hemisphere and their influence on variations in ionospheric parameters**

Based on the ECMWF ERA INTERIM and theoretical assessments, we found that baroclinic instability of regular air flow from the warm equator to the cold pole was the primary source of large-scale and medium-scale inhomogeneities in the winter stratosphere. This instability leads to a flow as a small number of jet streams (Fig. 28) which propagate eastward, under influence of Coriolis force, and form a spiral type circumpolar current providing top-down circulation of Brewer-Dobson in the stratosphere.

Shift instability of a jet stream generates the medium scale internal gravity waves (IGW) (Fig. 29) which can propagate upward to the mesosphere and to the lower thermosphere under certain conditions. We found that medium-scale IGWs (Fig. 29) generated by shift instability of a stratospheric jet current caused high variability of parameters of the winter mid-latitude ionosphere.

With increasing vertical velocity of a jet stream to 0.5-1 m/s, acoustic gravitational waves (AGWs) are generated (Fig. 30), which is a source of turbulent

mixing and air heating. This process is recorded as a sudden stratospheric warmings (SSWs).

EU-Russia cooperation in science yielded a mid-latitude network of ionosondes of vertical sounding almost completely covering the Eurasian continent along $\sim 55^\circ\text{N}$ (Figs. 28 and 31). Based on joint analysis of data from the ionosonde network, for the first time, we discovered sharp longitudinal variations in parameters of the ionosphere above active zones of stratospheric jet streams associated with vertical transfer of molecular gas in the lower thermosphere. The widest local variations in ionospheric parameters are observed when stratospheric circulation restructured during sudden stratospheric warmings (Fig. 31).

A decrease in electron density in the ionosphere is due to rising molecular gas and reduced $[\text{O}]/[\text{N}_2]$ is observed above jet stream, anticyclone, and the zone of stratospheric cyclone and anticyclone collision. Above cyclonic circulation, molecular gas descends from the lower thermosphere, with increasing electron density of ionospheric plasma. The difference of critical frequencies of the ionosphere above different jet stream zones can be 1–1.5 MHz.

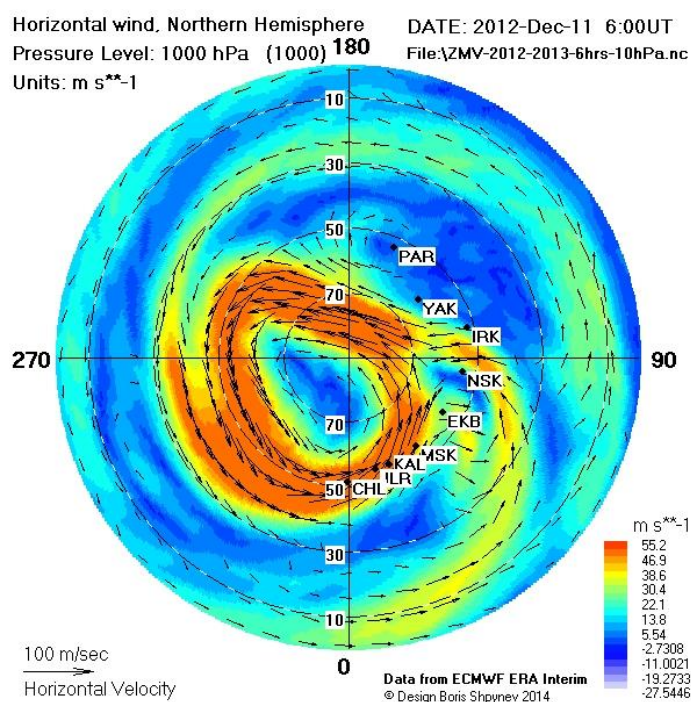


Fig. 28. Horizontal wind velocity at ~30km in the Northern Hemisphere on December 11, 2012.

As a result of baroclinic instability, a flow of warm air from the equator to the pole in the winter stratosphere develops as a small number of jet streams forming in a circumpolar vortex the polar region where cooling stratospheric air descends to the troposphere along a spiral trajectory. Large-scale vertical streams changing $[O]/[N_2]$ and electron density in the lower ionosphere form above different parts of a jet stream. According to the data from the mid-latitude network of ionosondes, critical frequency of the ionosphere above different circulation zones can differ to 1.5 MHz.

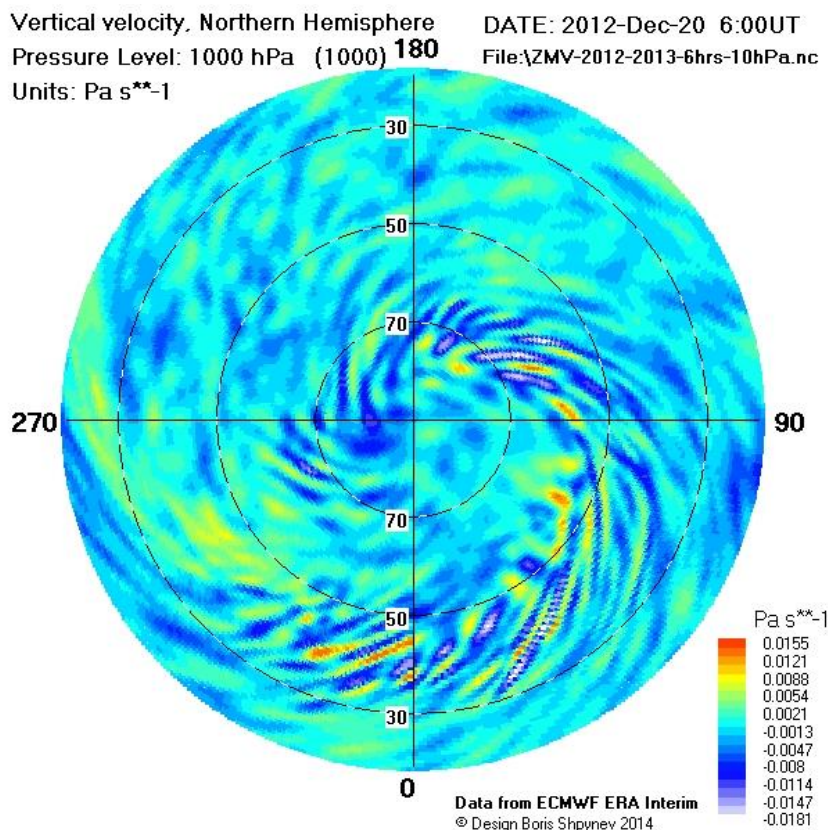


Fig. 29. December 20, 2012 vertical velocity in the Northern Hemisphere at ~30km.

Shift instability of a spiral type jet stream generates the medium scale internal gravity waves (IGWs) propagating upward. These IGWs are a primary source of medium-scale disturbances observed in the winter ionosphere.

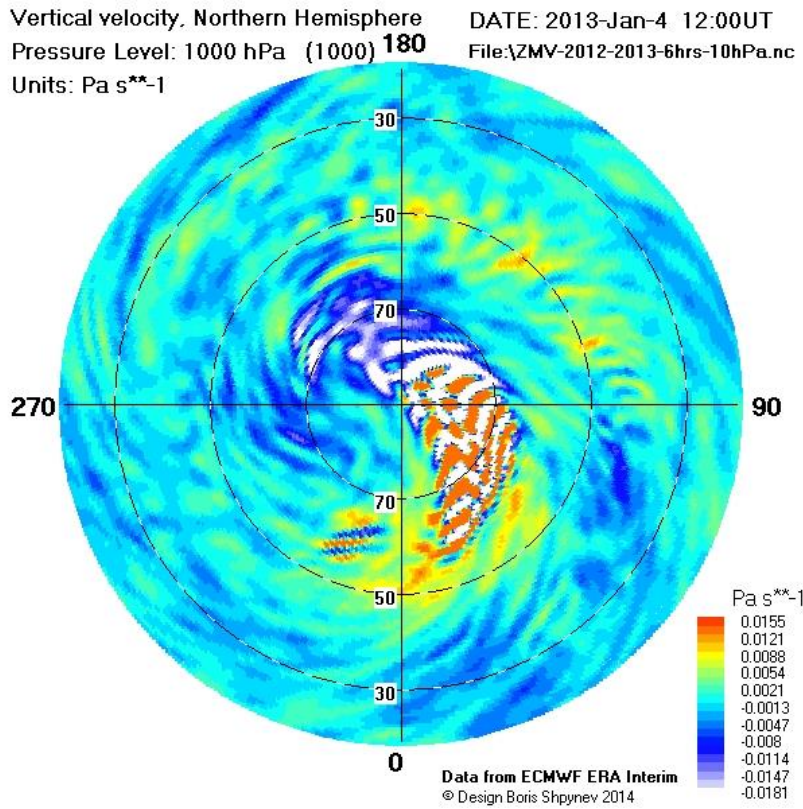


Fig. 30. January 4, 2013 vertical velocity in the Northern Hemisphere at ~30km.

With increasing vertical velocity of a descending stratospheric jet stream to 0.5–1 m/s, at the flow boundary shift instability generates small-scale acoustic gravitational waves converting flow energy into heat, which is recorded as sudden stratospheric warming (SSW).

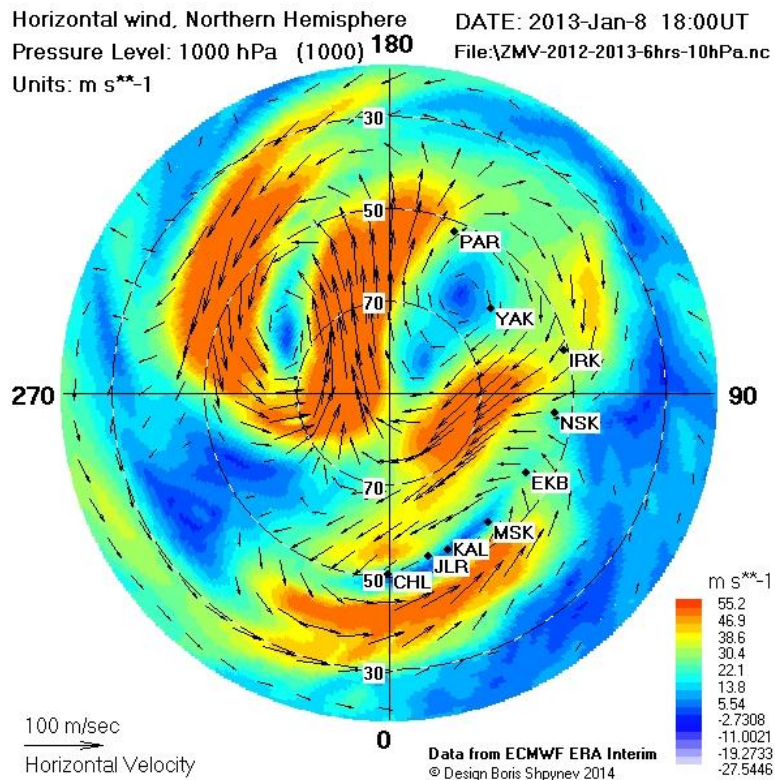


Fig. 31. January 8, 2013 horizontal wind velocity

A separation of the circumpolar vortex into pairs of cyclones and anticyclones is the final stage of development of stratospheric circulation during SSW. A decrease in the height of the ionosphere and increase in critical frequency are observed above cyclones. The ionosphere above anticyclone and the zone of

cyclone and anticyclone collision rises, and critical frequency of the ionosphere decreases.

Publications:

Shpynev B.G., Kurkin V.I., Ratovsky K.G., Chernigovskaya M.A., Belinskaya A.Yu., Grigorieva S.A., Stepanov A.E., Bychkov V.V., Pancheva D., Mukhtarov P.. High-midlatitude ionosphere response to major stratospheric warming / Earth, Planets and Space 2015, 67:18 (11 February 2015) doi:10.1186/s40623-015-0187-1.

Shpynev, B. G., Churilov S.M., Chernigovskaya M.A. Generation of waves by jet stream instabilities in winter polar stratosphere/mesosphere, // Journal of Atmospheric and Solar-Terrestrial Physics (2015), pp. 201-215 DOI:10.1016/j.jastp.2015.07.005.

Chernigovskaya M.A., Shpynev B.G., Ratovsky K.G. Meteorological effects of ionospheric disturbances from vertical radio sounding data // Journal of Atmospheric and Solar-Terrestrial Physics (2015), pp. 235-243 DOI:10.1016/j.jastp.2015.07.006.

2.2.2. Experimental research into manifestation of internal gravity waves in the upper Earth's atmosphere

We studied wave disturbances in the upper Earth's atmosphere, using the Irkutsk Incoherent Scatter Radar (IISR). A possibility of quick electron scanning of space, allowing us to obtain almost simultaneously height profiles of electron density ($N_e(h)$) in different directions, is an important advantage of the IISR over other radars of a similar type.

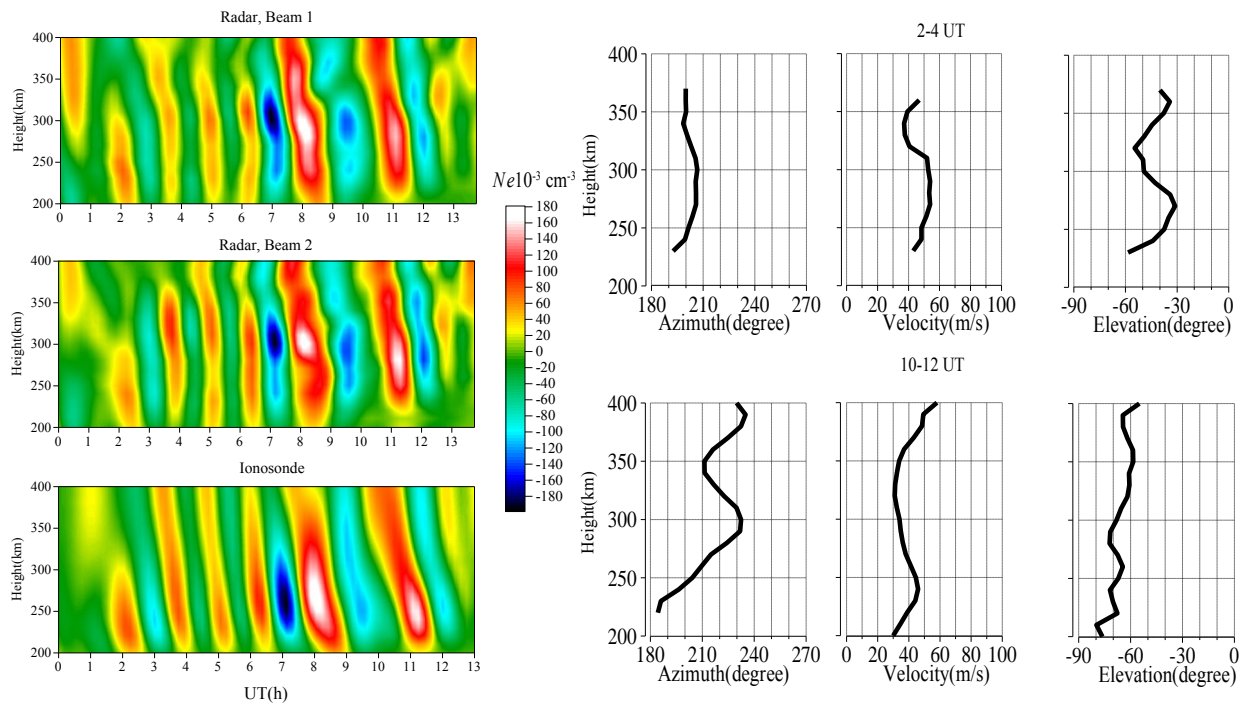


Fig. 32. Disturbances of electron density measured by three independent beams and TID propagation characteristics (in Russian).

We developed a method for cross-correlation analysis of disturbances in $N_e(h)$ different directions, which enabled us to reconstruct a three-dimensional space-time pattern of inhomogeneities, with full velocity vector of their displacement. Figure 32 shows disturbances $N_e(h)$ on three independent beams and TID propagation characteristics (azimuth, absolute value of velocity, and inclination angle to the horizon).

We developed an automated method for analysis of three-dimensional space-time inhomogeneities for analysis of long data series *for the first time*. We received sufficient statistics of propagation characteristics of traveling ionospheric disturbances (TIDs) with periods of from 1 to 6 hours in the upper atmosphere (Fig. 33). We found that TIDs mostly propagated from the north to the south and from the south to the north.

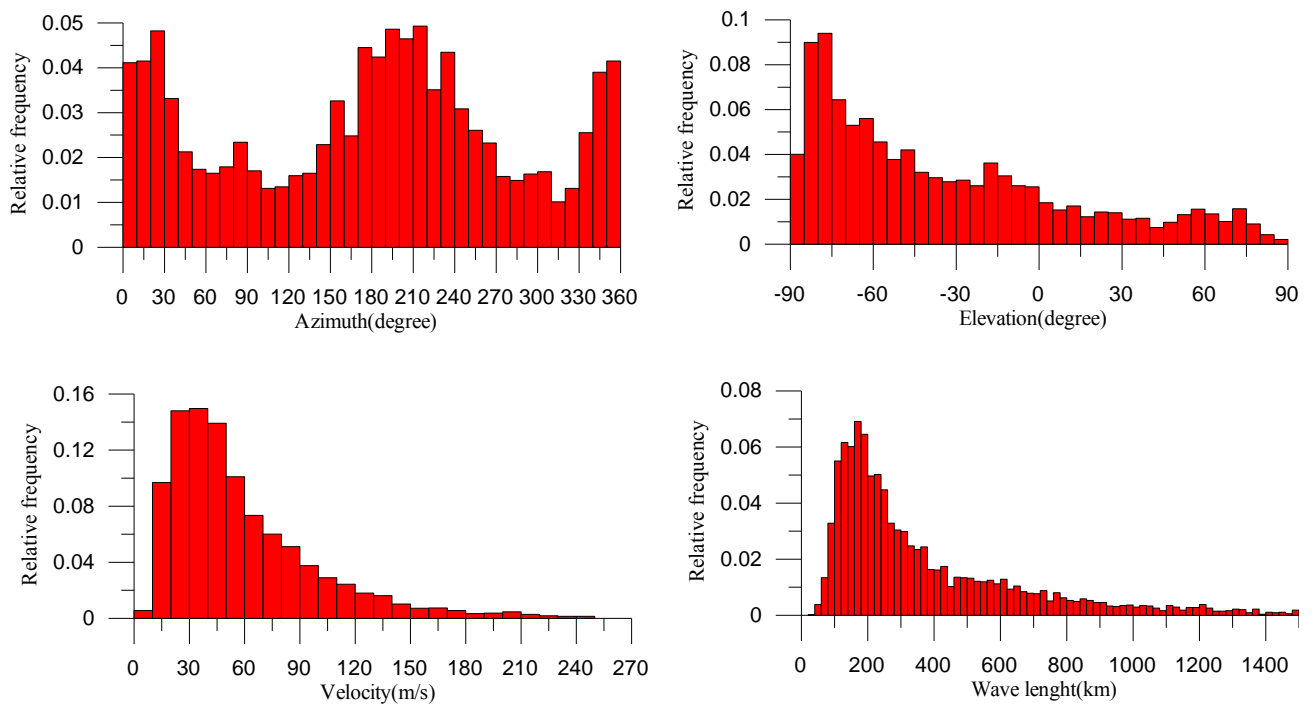


Fig. 33. Distributions of TID propagation characteristics.

The range of $\sim 25\text{--}50$ m/s contains a maximum in the distribution of absolute values of TID velocity; the range of 150–200 km, a maximum in their wavelength distribution. Around 75% of disturbances have a negative inclination angle of the wave front to the horizon.

Using data on full three-dimensional TID velocity vector, we checked TID characteristics to ensure a match with known Hines's dispersive correlation for internal gravity waves (IGWs) in the atmosphere (Fig. 34). Simulation showed that more than 70% of the observed TIDs supported the theoretical notions of IGW propagation in the upper atmosphere, considering a possible effect of neutral wind.

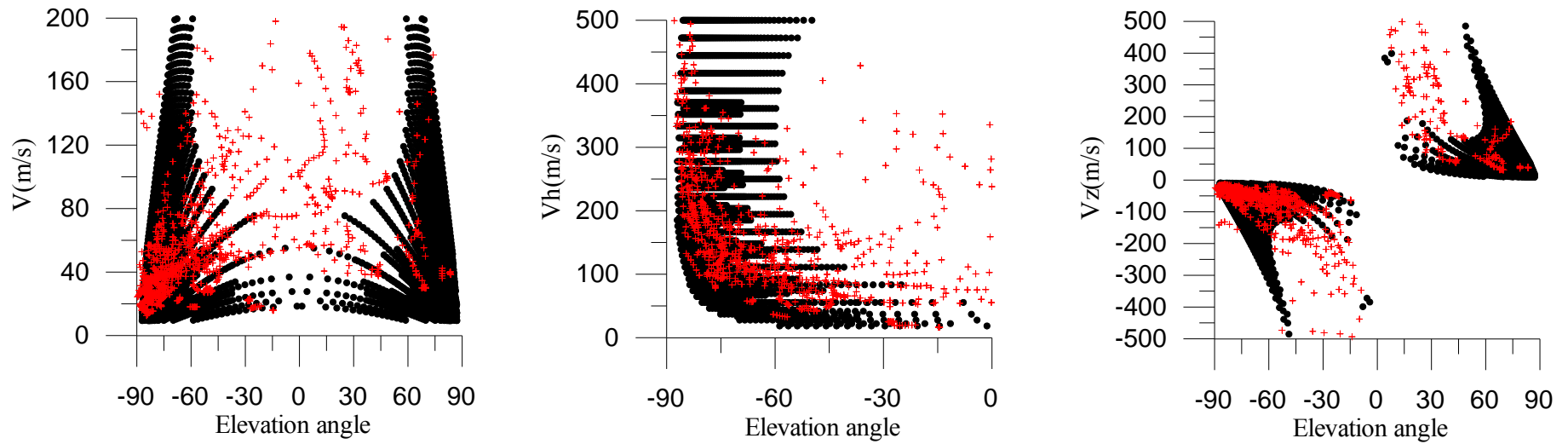


Fig. 34. The dependences of TID velocities on the inclination angle (V is the absolute value of velocity; V_h , horizontal velocity; V_z , vertical velocity). The red crosses mark observational results; the black dots, simulation results (wind velocity changed from -300 to +300 m/s, the observed period was from 1 to 3 hours, horizontal wave number was from 100 to 2 000 km).

Having analyzed three-dimensional characteristics of the observed IGWs, **for the first time** we proposed a method for determination of monthly average diurnal variations in meridional and zonal wind velocities where the values of wind components at any given time point t were defined as a functional minimum:

$$\sum (U_x \sin(\varphi_i) + U_y \cos(\varphi_i) - U_i)^2 \rightarrow \min ,$$

where U_x is the zonal wind; U_y , the meridional wind; U_i , the horizontal wind along the direction of IGW propagation; φ_i , the azimuth. Figure 35 illustrates the wind parameters at IGW observation heights (220–250 km) for winter. The red line corresponds to the values predicted using the HWM2007 model; the black line, the results using the developed method. The positive meridional wind velocity is southward; the positive zonal wind velocity, eastward.

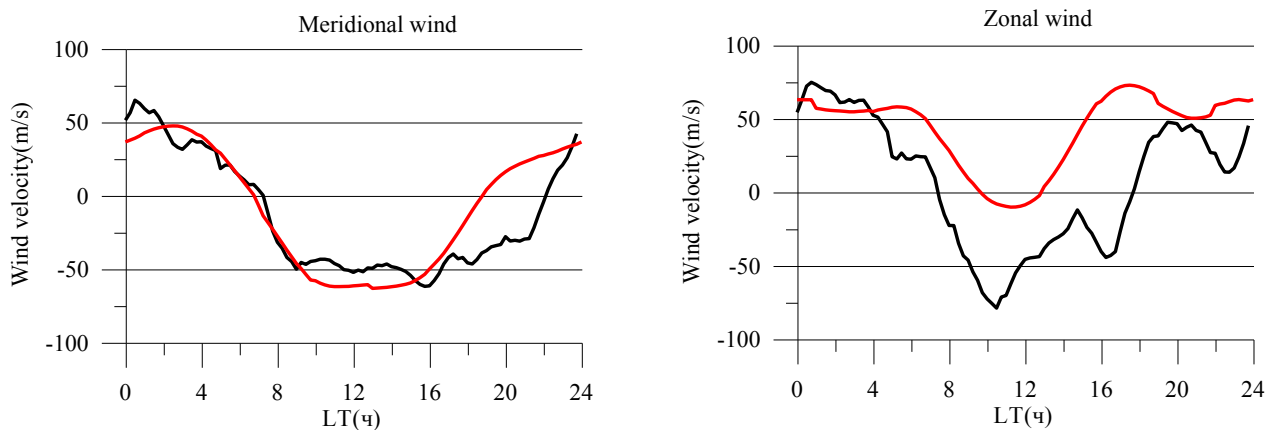


Fig. 35. Monthly average diurnal variations in meridional (left) and zonal (right) wind velocities.

For the first time, we analyzed azimuth distribution of IGWs with different inclination angles of the wave front to the horizon. The majority of IGWs have a downward phase velocity (a negative inclination angle of the wave front), which corresponds to waves propagating from the source lying under the observation

region. IGWs with inclination angles of the wave front take up to 25% of all observations and can be conveniently divided into two ranges: 0° – 45° waves whose nature is associated with reflection of primary IGWs at the regions of sharp change in wind direction located above the observation point ($\sim 15\%$) and 45° – 90° waves from the sources above the region under consideration ($\sim 10\%$). Fig. 36 shows the azimuth distribution of these two IGW types. Red color marks sectors where projection of wind calculated using the HWM2007 model on IGW propagation direction is more than 50m/s. We assume that such wind can prevent IGW propagation, i.e., the so-called wind filtration must occur.

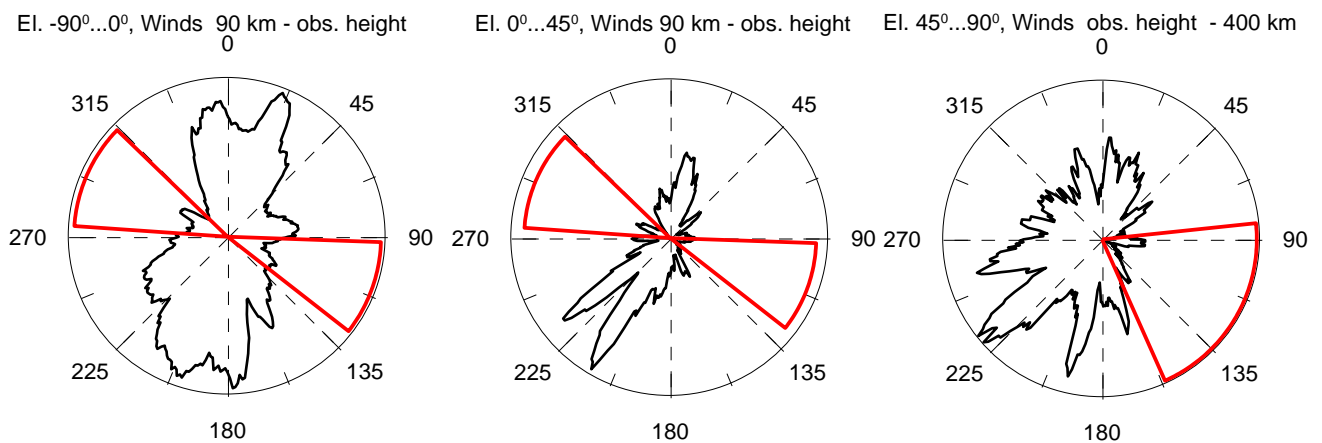


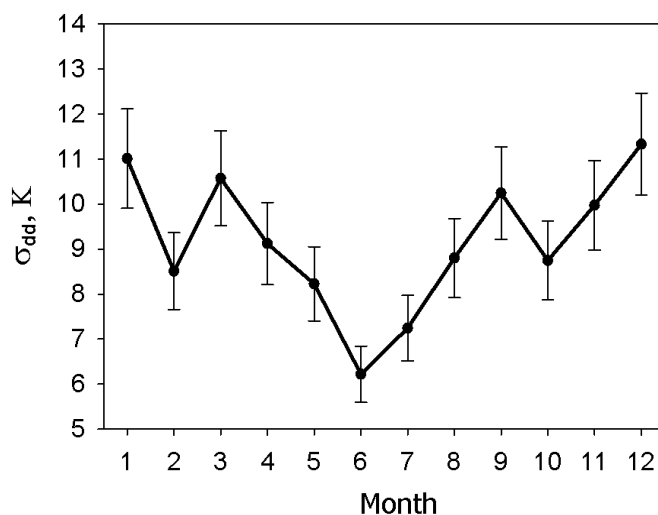
Fig. 36. Black color shows azimuth distributions of IGWs propagating from a source lying below the observation region (left), IGWs reflected at the boundary of rapid wind direction change (center), and IGWs propagating from a source lying above the observation region (right). Red color denotes sectors where wind projection on IGW propagation direction is more than 50m/s.

The different paths of these three types of IGWs in the upper atmosphere conditions different wind filtration. The azimuth distribution of the reflected IGWs repeats that of the primary waves, but is narrower, first, because these waves underwent double filtration by neutral wind and, second, because reflection conditions were not observed for all the primary waves. The azimuth distribution of IGWs having sources lying above the region consideration is the widest because these waves have the shortest path to the region of their observation.

2.3. Atmospheric research

2.3.1. Study of variability of parameters of the neutral upper atmosphere and ionosphere from spectrometric measurements and radio sounding data

We developed a method for comprehensive analysis of atmospheric and ionospheric variability allowing us to receive information about dynamics of different atmospheric regions. We proposed using temperature variability at the mesopause received from spectrometric measurements of hydroxyl molecule emission (maximum emission height of ~87 km) as a parameter of atmospheric variability to compare variations in ionospheric parameters. Interdiurnal and intradiurnal variations in temperature at the mesopause are mainly conditioned by wave processes, namely, planetary waves, tides, and internal gravity waves; therefore, comparison of temperature variability to that of ionospheric parameters allows us to quantify manifestation of wave activity of different time scale in variations in parameters of the neutral upper atmosphere and ionosphere.



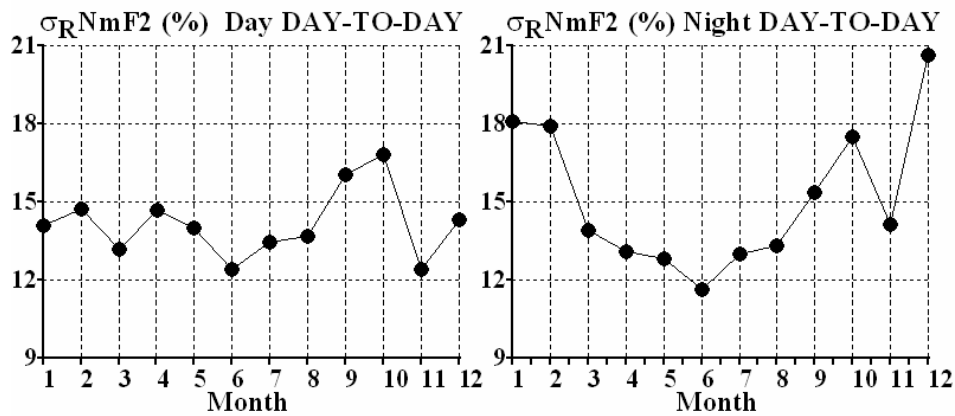


Fig. 37. Top panel: the seasonal variations in monthly average deviations of the mesopause temperature (T_{dd}) from its annual variations. Bottom panel: the seasonal variations in interdiurnal variability of F2 peak electron density σ_{RNmF2} for day (left) and night (right) conditions.

According to multi-year spectrometric measurements and vertical radio sounding data, using the proposed method, we studied seasonal variations in variability of parameters of the neutral upper atmosphere (mesopause temperature, T_m) and ionosphere (F2 peak electron density, NmF2) caused by manifestation of wave activity of different time scale. We revealed seasonal dependences of variations in these parameters (Fig. 37). The seasonal variations in interdiurnal variability of T_m and NmF2 have a similar character: the maximum values are observed in the winter months and equinox periods when the seasonal restructuring of atmospheric circulation occurs. This fact can indicate that planetary waves propagating from the lower atmosphere have a significant influence on a temperature regime at the mesopause, as well as on behavior of electron density in the F2 region of the ionosphere.

Publications:

Medvedeva, I., and K. Ratovsky (2015), Studying atmospheric and ionospheric variabilities from long-term spectrometric and radio sounding measurements, *J. Geophys. Res. Space Physics*, 120, Issue 6, pp. 5151–5159, doi:10.1002/2015JA021289.

2.3.2. Comprehensive analysis of disturbances of parameters of the neutral atmosphere and ionosphere in the Eastern Siberia during January 2013 sudden stratospheric warming

We conducted a comprehensive analysis of parameters of the neutral atmosphere and ionosphere as deduced from ground-based spectrometric measurements and radio sounding data with the use of the ISTP SB RAS instruments along with MLS Aura and reanalysis data during development of January 2013 sudden stratospheric warming (SSW). This was a major stratospheric warming accompanied by a change in zonal circulation to 60N at the level of 10 GPa from western to eastern one, which occurred on January 5–6 with a separation of a circumpolar vortex.

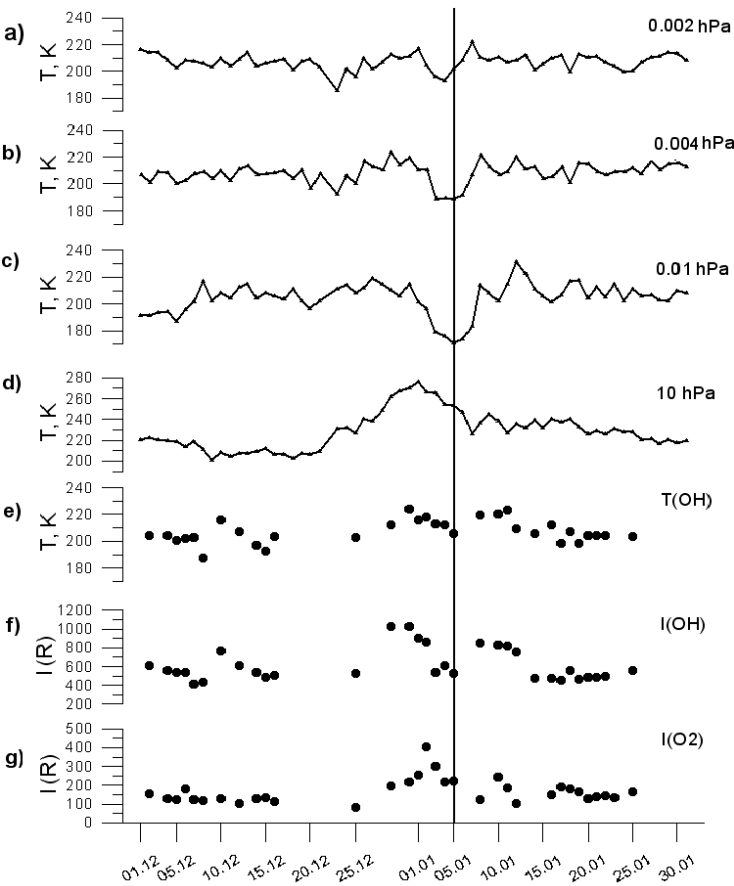


Fig. 38. The temperature variations in the mesosphere and lower thermosphere (MLT, a-c) and in the stratosphere (d) from MLS Aura data; the variations in OH rotational temperature (e) and intensities of OH (f) and O₂ (g) emissions from on ground-based spectrometric data from December 1, 2012 to January 31, 2012. The vertical line denotes the onset of the major SSW.

We revealed and analyzed SSW manifestations in the range of heights from the stratosphere to the thermosphere above the Eastern Siberia which was close to the region of the largest temperature anomalies associated with SSW in the middle stratosphere (Fig. 38). In the course of SSW development, increase in stratospheric temperature was accompanied by cooling of the mesosphere observed in a sufficiently narrow layer.

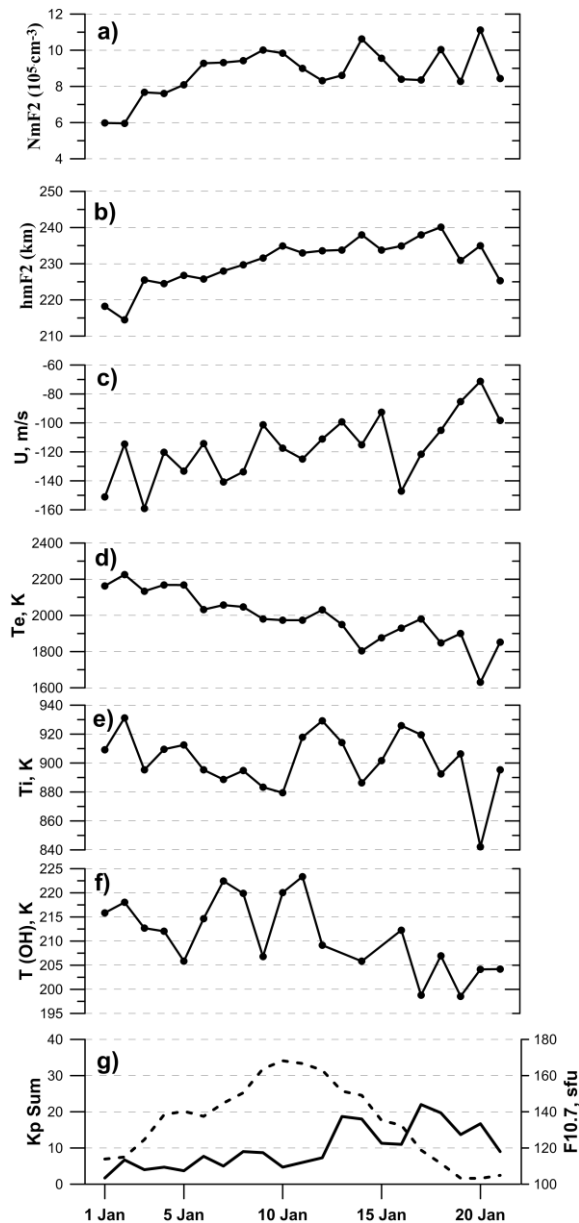


Fig. 39. The daily values of the ionospheric parameters during January 1–21, 2013:

a) peak electron density (NmF2); b) F2 maximum ionization height (hmF2); c) neutral meridional wind velocity at 266 km, “-” is the south-north direction; d) electron temperature at 266 km; e) ion temperature at 266 km; f) interdiurnal variations in OH rotational temperature at ~87 km; g) geomagnetic (solid line) and solar (dashed line) activity variations.

For the first time, we obtained experimental evidence of enhancement of vertical transfer of main atmospheric components from underlying atmospheric layers to the upper atmosphere. The enhancement was caused by stratospheric warming. This resulted in 2-2.5 times significantly intensified ON and O2 emissions in the MLT (Fig. 38 f-g) due to increasing oxygen concentration at airglow heights and in violated relation of electron density and the F2 region maximum ionization height of the ionosphere (Fig. 39 a-b) due to increasing molecular density and O2 and N2 molecules thermospheric heights. We discovered that behavior of ion temperature in the F2 region (Fig. 39e) largely repeated variations in temperature of the neutral atmosphere in the MNT (Fig. 39f) with a time delay of several days (~5 days).

Publications:

Medvedeva, I., Medvedev, A., Ratovsky, K., Shcherbakov, A., Tolstikov, M. Comprehensive study of disturbances of the neutral atmosphere and ionosphere parameters over Eastern Siberia during the 2013 January major sudden stratospheric warming // *Advances in Space Research* Volume 56, Issue 9. 2015. P. 1877–1885, <http://dx.doi.org/10.1016/j.asr.2015.06.008>.

Vargin P. N., Medvedeva I.V. Study of a temperature and dynamic regime of the extratropical atmosphere in the Northern Hemisphere during sudden stratospheric warming in winter 2012-2013 (in Russian) // The Izvestiya RAN. Atmospheric and Oceanic Physics, 2015, V. 51, N. 1. Pp. 20–38. DOI: 10.7868/S0002351514060170.

2.3.3. Solar effects on climatic characteristics

Based on comprehensive analysis of observational data and a model for solar effects on climatic characteristics developed by the ISTP SB RAS, we revealed the main mechanisms and physical processes responsible for observed regional and global climate changes. These factors make a major contribution to climate change: variations in the solar activity level, efficiency of heat exchange in the atmosphere–ocean–dry land which is determined by changes in wind stress. Deep ocean circulation and vertical mixing in the Ocean significantly influence on heat exchange. The long-term changes in sea-ice extent also significantly affect temperature and heat content of the Global Ocean, i.e., on climate change.

We established that the climatic response was characterized by significant space-time inhomogeneity, was regional, and depended on the climate epoch (Fig. 40).

In the period of the first warming (1910–1948), sea surface temperature (SST) response to solar activity effects was global (Fig. 40b). In this epoch, increase in geomagnetic activity is characterized by a significant positive trend which was maximum for the time interval from 1868 to 2015 under consideration.

We found the regions where the long-term temperature changes were determined mainly by solar activity variations. Fig. 41 shows long-term SST variations in one of these regions.

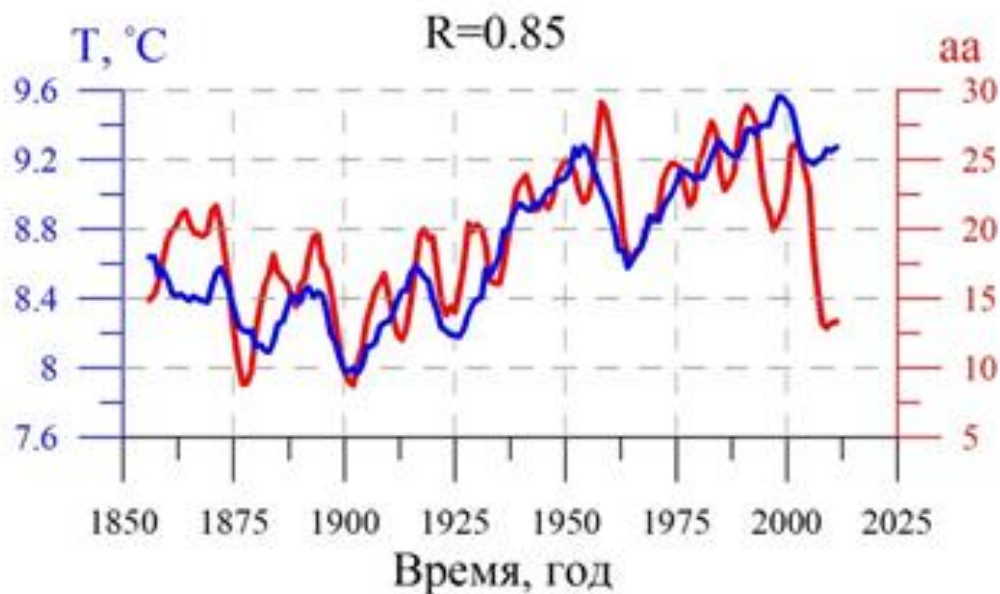


Fig. 41. The long-term variations in SST in the Indian Ocean (40S–50S; 30E–60E) and geomagnetic activity.

Publications:

Zherebtsov G.A., Kovalenko V.A. Influence of Solar Activity on the Climate Change, *Atmospheric and Oceanic Optics.*, 27 (6), 506-510 (2014).

Zherebtsov G.A., Kovalenko V.A., Kirichenko K.E. Main physical processes and mechanisms responsible for the observable climate changes in the 20-21st centuries // *Proc. SPIE.* 2015. V. 9680. P. 968057. doi: 10.1117/12.2205740.

Kirichenko K.E., Kovalenko V.A., Molodykh S.I. Manifestation of Solar Activity in Global Sea Surface Temperature (in Russian) // *Atmospheric and Oceanic Optics.* 2014. V. 27. No 2. Pp. 154–157

Kirichenko K.E., Belousova E.P., Kovalenko V.A. Wind-stress effect on the relationships between sea surface temperature and geomagnetic activity // *Proc. SPIE.* 2015. V. 9680. P. 96805T, doi: 10.1117/12.2205318

Contacts:

Scientific Secretary of the ISTP, I.I. Salakhutdinova, Cand. Sc. (Phys.&Math)
 e-mail: isalakh@iszf.irk.ru, тел.: (3952) 42-59-19, cell phone number: 89149380801.